

1 **A Regional multi-Air Pollutant Assimilation System (RAPAS v1.0)**
2 **for emission estimates: system development and application**

3 Shuzhuang Feng¹, Fei Jiang^{1,2}, Zheng Wu³, Hengmao Wang^{1,2}, Wei He¹, Yang Shen¹,
4 Lingyu Zhang¹, Yanhua Zheng¹, Chenxi Lou¹, Ziqiang Jiang⁴, Weimin Ju^{1,2}

5
6 ¹ *Jiangsu Provincial Key Laboratory of Geographic Information Science and Technology, International*
7 *Institute for Earth System Science, Nanjing University, Nanjing, 210023, China*

8 ² *Jiangsu Center for Collaborative Innovation in Geographical Information Resource Development and*
9 *Application, Nanjing, 210023, China*

10 ³ *Chongqing Institute of Meteorological Sciences, Chongqing, 401147, China*

11 ⁴ *Jiangsu Environmental Monitoring Center, Nanjing, 210019, China*

12
13
14
15
16 *Correspondence to: Fei Jiang (jiangf@nju.edu.cn)*

30 Abstract

31 Top-down atmospheric inversion infers surface-atmosphere fluxes from spatially
32 distributed observations of atmospheric compositions, which is a vital means for
33 quantifying large-scale anthropogenic and natural emissions. In this study, we
34 developed a Regional multi-Air Pollutant Assimilation System (RAPAS v1.0) based on
35 the Weather Research and Forecasting/Community Multiscale Air Quality Modeling
36 System (WRF/CMAQ) model, the three-dimensional variational (3DVAR) algorithm
37 and the ensemble square root filter (EnSRF) algorithm. It is capable of simultaneously
38 ~~assimilating to simultaneously assimilate~~ spatially distributed hourly in-situ
39 measurements of CO, SO₂, NO₂, PM_{2.5} and PM₁₀ concentrations to quantitatively
40 optimize gridded emissions of CO, SO₂, NO_x, primary PM_{2.5} (PPM_{2.5}) and coarse PM₁₀
41 (PMC) on regional scale. RAPAS includes two subsystems, initial field assimilation (IA)
42 subsystem and emission inversion (EI) subsystem, which are used to generate a good
43 ~~“perfect”~~ chemical initial condition (IC), and conduct inversions of anthropogenic
44 emissions, respectively. A “two-step” inversion scheme is adopted in the EI subsystem
45 ~~in each data subsystem in its each data~~ assimilation (DA) window, in which the emission
46 is inferred in the first step, and then, it is input into the CMAQ model to simulate the
47 initial field of the next window, meanwhile, it is also transferred to the next window as
48 the prior emission. The chemical IC is optimized through the IA subsystem, and the
49 original emission inventory is only used in the first DA window. Besides, a “super-
50 observation” approach is implemented based on optimal estimation theory to decrease
51 the computational costs and observation error correlations and reduce the influence of
52 representativeness errors.

53 With this system, we estimated the emissions of CO, SO₂, NO_x, PPM_{2.5} and PMC in
54 December and July 2016 over China using the corresponding nationwide surface
55 observations. The 2016 Multi-resolution Emission Inventory for China (MEIC 2016)
56 was used as the prior emission. For December, tThe system was run from 26 November
57 to 31 December, in which the IA subsystem was run in the first 5 days, and the EI
58 subsystem was run in the following days. In July, the system was run in the same way.

59 ~~The evaluation and sensitivity testing of this system mainly focused on December. The~~
60 ~~optimized ICs at the first 5 days and the posterior emissions in December were~~
61 ~~evaluated against the assimilated and independent observations.~~ Results showed that
62 ~~the simulated concentrations of CO, NO₂, SO₂, PM_{2.5} and PM₁₀ with the prior inventory~~
63 ~~have large systematic biases, with relative biases in the range of -48.2-54.2%. In the IA~~
64 ~~subsystem, after 3DVAR, –the root mean squared error (RMSE) of the simulated~~
65 ~~concentrations decreased by 50.0-73.2%, and the correlation coefficient (CORR)~~
66 ~~increased to 0.78-0.92 for the five species compared to the simulations without 3DVAR.~~
67 ~~In the EI subsystem, after emission inversions. Additionally, the RMSE of the simulated~~
68 ~~concentrations decreased by 40.1-56.3%, and the CORR increased to 0.69-0.87~~
69 ~~compared to the simulations without optimized emissions.~~ For the whole mainland
70 China, the uncertainties were reduced by 44.4%, 45.0%, 34.3%, 51.8% and 56.1% for
71 CO, SO₂, NO_x, PPM_{2.5} and PMC, respectively. Overall, compared to the prior emission
72 (MEIC 2016), the posterior emissions increased by 129%, 20%, 5%, and 95% for CO,
73 SO₂, NO_x and PPM_{2.5}, respectively, indicating that there was significant
74 underestimation in the MEIC inventory. The posterior PMC emissions, including
75 anthropogenic and natural dust contributions, increased by 1045%. A series of
76 sensitivity tests were conducted with different inversion processes, prior emissions,
77 prior uncertainties, and observation errors. Results showed that the “two-step” scheme
78 clearly outperformed the simultaneous assimilation of ICs and emissions (“one-step”
79 scheme), and the system is rather robust in estimating the emissions using the
80 nationwide surface observations over China. Our study offers a useful tool for
81 accurately quantifying multi-species anthropogenic emissions at large scales and near-
82 real time.

83

84

85

86

87 **1. Introduction**

88 Due to rapid economic developments and pollution control legislations, an increasing
89 demand to provide updated emission estimates has arisen, especially in areas where
90 anthropogenic emissions are intensive. Accurately estimating source emission
91 quantities and spatiotemporal changes resulting from various regulations is imperative
92 and valuable for understanding air quality responses and crucial for providing timely
93 instructions for the design of future emissions regulations. However, most inventories
94 have been developed based on a bottom-up approach and are usually updated with a
95 few years delay due to the complexity of gathering all statistical information on activity
96 levels and sector-specific emission factors (Ding et al., 2015). The large uncertainty
97 associated with the low temporal and spatial resolution of these datasets also greatly
98 limits the assessment of emission changes. Some studies (Bauwens et al., 2020; Shi and
99 Brasseur, 2020) have evaluated emission changes indirectly through concentration
100 measurements, but air pollution changes are not only dominated by emission changes,
101 but also highly affected by meteorological conditions (Shen et al., 2021).

102 Top-down atmospheric inversion infers surface-atmosphere fluxes from spatially
103 distributed observations of atmospheric compositions. Recent efforts have focused on
104 developing air pollution data assimilation (DA) system to conduct the top-down
105 inversion, which is able to integrate model and multi-source and large amounts
106 of observational information to constrain emission sources. Two major methods,
107 namely, 4D-variational data assimilation (4DVAR) and ensemble Kalman filter (EnKF),
108 are widely used in those DA systems. 4DVAR provides a global optimal analysis
109 through minimizing a cost function. It shows implicit flow-dependent background error
110 covariance and can reflect complex nonlinear constraint relationship (Lorenc, 2003).
111 Additionally, the model error can be partly accounted for with a weak constraint
112 4DVAR method through the definition of a systematic error term in a cost function
113 (Derber, 1989). For example, GEOS-Chem and TM5 4DVAR frameworks have been
114 used to estimate CH₄ (Alexe et al., 2015; Schneising et al., 2009; Stanevich et al., 2021;
115 Wecht et al., 2014) and CO₂ fluxes (Basu et al., 2013; Nassar et al., 2011; Wang et al.,

116 2019a) from different satellite retrieval products. Monteil et al. (2013) showed that the
117 global patterns of CH₄ emissions derived from SCIAMACHY (with bias correction)
118 and GOSAT retrievals are in remarkable agreement based on 15 months observations.
119 ~~Additionally, For example, _~~Jiang et al. (2017) used 4DVAR algorithm to estimate
120 global CO emission trends from 2000–2015 using MOPITT retrievals. Kurokawa et al.
121 (2009) and Stavrakou et al. (2008) also used 4DVAR technique to estimate NO_x
122 emission changes. However, the drawback of the 4DVAR method is the additional
123 development of adjoint models that are technically difficult and cumbersome for
124 complex chemical transport models. Instead, EnKF uses the flow-dependent
125 background error covariance generated by ensemble simulations to map the deviations
126 in concentrations to increments of emissions, which is more flexible and easier to
127 implement. Many previous studies have used EnKF techniques to assimilate the single
128 or dual species observations to optimize the corresponding emission species (Chen et
129 al., 2019; Peng et al., 2017; Schwartz et al., 2014; Sekiyama et al., 2010). Multispecies
130 data assimilation has shown the advantage of efficiently reducing the uncertainty in
131 emission inventories and has led to improvements in air quality forecasting (Ma et al.,
132 2019; Miyazaki et al., 2012b), since it would offer additional constraints on emission
133 estimates through the improvements in related atmospheric fields, chemical reactions,
134 and gas-particle transformations (Miyazaki and Eskes, 2013). Barbu et al. (2009)
135 updated sulfur oxide (SO_x) emissions with SO₂ and sulfate aerosol observations and
136 found that simultaneous assimilation of both species had better performance than
137 assimilating one of them alone.~~Barbu et al. (2009) updated sulfur oxide (SO_x) emissions~~
138 ~~with SO₂ gas and sulfate aerosol observations and showed that forecasts were improved~~
139 ~~overall but degraded when derived only from SO₂ or sulfate observations.~~

140 The deviation in chemical initial condition (IC) is one of the important sources of error
141 that affects the accuracy of emission inversion, because ~~atmospheric~~atmospheric
142 inversion fully attributes the biases in simulated and observed concentrations to the
143 deviations in emissions (Meirink et al., 2006; Peylin et al., 2005). The biases of
144 concentrations would be compensated through unreasonable adjustment of pollution

145 emissions without the optimization of ICs (Tang et al., 2013). Tang et al. (2011) reported
146 that the simultaneous optimizations of the ICs of O₃, NO_x and volatile organic
147 compounds (VOCs) and the emissions of NO_x and VOCs produced an overall better
148 performance in ozone forecasts than the adjustment in emissions only. Similar method
149 of simultaneously optimizing chemical ICs and emissions were also applied to
150 constraining emissions in many previous studies (Ma et al., 2019; Miyazaki et al., 2012a;
151 Peng et al., 2018). Although a large improvement has been achieved, this method still
152 has great limitations because the contributions from the emissions and the chemical ICs
153 to the model's bias are difficult to distinguish (Jiang et al., 2017). ~~Besides, the~~
154 ~~simultaneous optimization means that assimilation window is independent with each~~
155 ~~other, generally, the uncertainties of the emissions cannot be fully corrected in time in~~
156 ~~a window, resulting in an accumulation of errors in the estimation (Jiang et al., 2021).~~In
157 addition, in this method, the constraints of the chemical ICs with observations in each
158 assimilation window make the emission inversions are independent between
159 assimilation windows, means if the emission in one window is overestimated or
160 underestimated, it cannot be transferred to the next window for further correcting and
161 be compensated in the following windows. This may result in a systematic bias in the
162 inverted emissions (Jiang et al., 2021).

163 Since 2013, China has deployed an air pollution monitoring network that publishes
164 nationwide and real-time hourly surface atmospheric observations. This dataset
165 provides an opportunity to improve emission estimates using DA. In this study, a
166 regional multi- air pollutant assimilation system introducing 3DVAR and EnKF DA
167 techniques is constructed to simultaneously assimilate various surface observations
168 (e.g., CO, SO₂, NO₂, O₃, PM_{2.5} and PM₁₀). Considering the possible shortcomings of
169 the simultaneous optimization method (named as “one-step” method in this study) as
170 mentioned by Jiang et al. (2021), we adopted a “two-step” method (Sect. 3) in this system.
171 Unlike the “one-step” method, the ICs of each DA window in the “two-step” method is
172 simulated using the posterior emissions of the pervious DA window. Against the
173 ~~limitations of the simultaneous optimization of emissions and chemical ICs in each DA~~

174 ~~window (here, named as “one-step” method), a “two-step” approach (Sect. 3) is~~
175 ~~performed, in which the IC of each DA window is simulated using the posterior~~
176 ~~emission of the pervious DA window.~~ The capability of RAPAS in reanalysis field
177 generation and emission inversion estimation is-was evaluated. The robustness of the
178 system is-was also investigated with different prior inventories, uncertainty settings of
179 the prior emission, and observation errors. This paper is organized as follows: in Sect.
180 2, we introduce the DA system and the observation data, and in Sect. 3, we describe the
181 experimental design. The results of the system performance and sensitivity ~~runs-tests~~
182 are presented and discussed in Sect. 4, followed by the conclusions in Sect. 5.

184 2. Method and data

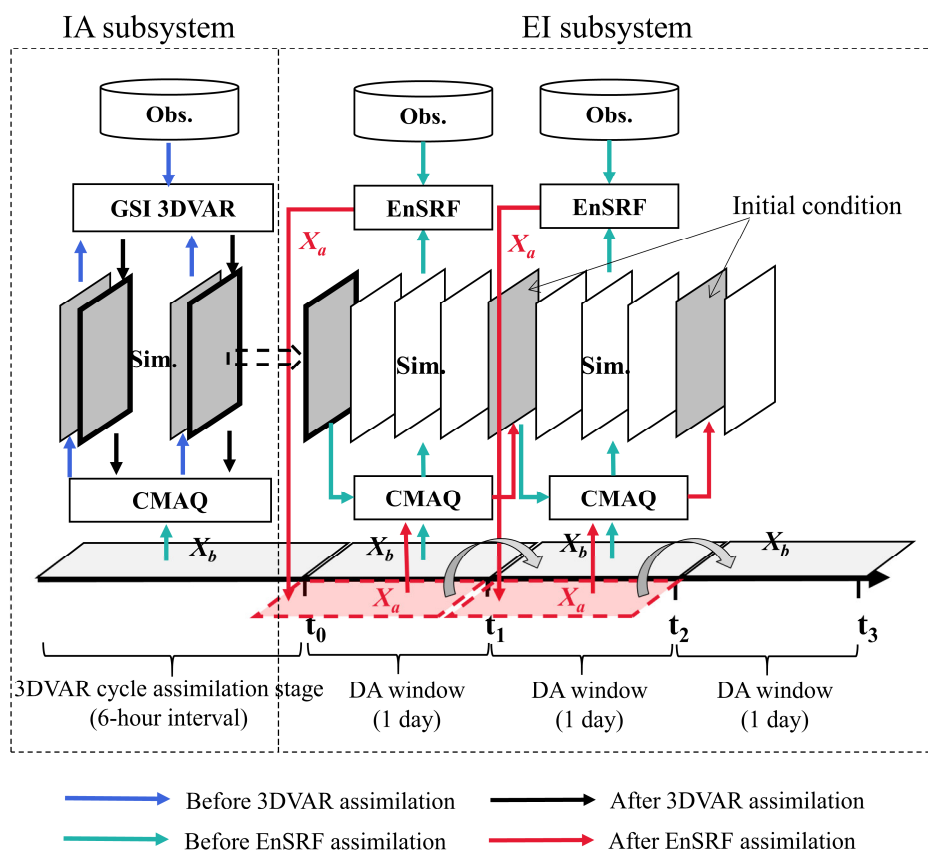
185 2.1 System description

186 2.1.1 Procedure of the assimilation system

187 A regional air pollutant assimilation system has been preliminarily constructed and
188 successfully applied in our previous studies to optimize gridded CO and NO_x emissions
189 (Feng et al., 2020a; Feng et al., 2020b). Herein, the system is-was further extended to
190 simultaneously assimilate multiple species (e.g., CO, SO₂, NO₂, O₃, PM_{2.5} and PM₁₀)
191 and officially named as the Regional multi- Air Pollutant Assimilation System
192 (RAPASv1.0). The RAPAS mainly includes three components: a regional chemical
193 transport model (CTM), which is coupled offline and used to simulate the
194 meteorological fields and atmospheric compositions, and the 3DVAR and ensemble
195 square root filter (EnSRF) modules, which are used to optimize chemical ICs (Feng et
196 al., 2018; Jiang et al., 2013**b**) and anthropogenic emissions (Feng et al., 2020a; Feng et
197 al., 2020b), respectively. The introduction of 3DVAR mainly considers its great
198 performance based on our previous study and lower computational cost during spin-up
199 period in optimizing ICs. Additionally, it has been found that the 3DVAR method can
200 obtain a better initial field than the EnKF method (Schwartz et al., 2014).

201 Based on above three components, the RAPAS is divided into two subsystems, namely

202 the IC assimilation (IA) subsystem (CTM plus 3DVAR) and the emission inversion (EI)
203 subsystem (CTM plus EnSRF). As shown in Figure 1, the IA subsystem is first run
204 ~~separately~~ to optimize chemical ICs ~~using the CTM model and cycling assimilation~~
205 ~~within the 3DVAR framework~~ (Kleist et al., 2009; Wu et al., 2002) for the subsequent
206 EI subsystem. In the IA subsystem, we do not need to distinguish the type of sources of
207 the model-observation mismatch error. It runs only once and provides a “perfect”
208 chemical ICs for the subsequent EI subsystem. The EI subsystem runs cyclically with
209 a “two-step” scheme, and in each cycle (DA window), we use a “two-step” calculation
210 scheme. In the first step, the prior emissions (X^b) are perturbed and put into the CTM
211 model to simulate chemical concentration ensembles, ~~which are then sampled~~
212 ~~according to the locations and times of the observations.~~ The simulated concentrations
213 of the lowest model level are then interpolated to the observation space according to
214 the locations and times of the observations using the nearest neighbor interpolation
215 method. The prior emissions (X^b), simulated observations and real observations
216 ~~sampled data together with observations and prior emission ensembles~~ are entered into
217 the EnSRF ~~module~~algorithm to generate the optimized emissions (X^a). In the second
218 step, the optimized emissions are entered ~~again~~ into the CTM model again to generate
219 the initial fields of the next DA window. Meanwhile, the optimized emissions are
220 transferred to the next window as the prior emissions, ~~which means that the original~~
221 ~~emission inventory is only used in the first DA window in the EI subsystem.~~ Different
222 from the ~~synchronously scheme (“one-step” scheme), which only runs the model once~~
223 ~~and optimizes the ICs of the next window and emission at the same time,~~ this “two-
224 step” scheme needs to run the ~~simulations~~CTM model twice, which is time consuming,
225 but it could transfer the potential errors of the inverted emissions in one DA window to
226 the next for further correction. ~~but it could transfer the errors in the inverted emissions~~
227 ~~of current DA window to the next one for further correction.~~ The benefit of this scheme
228 will be further presented in Sect. 4.3.



229

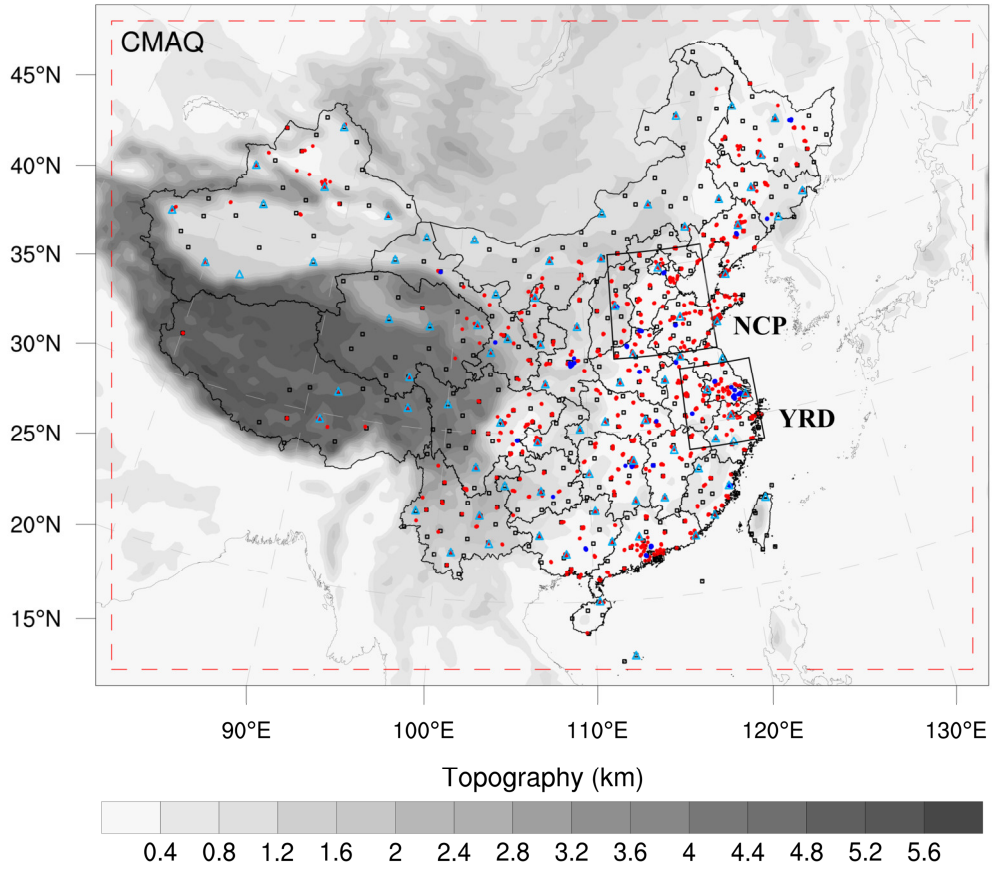
230 **Figure 1.** The composition and flow chart of RAPAS. The x_a and x_b represent the
 231 prior and posterior emissions. The 3DVAR assimilation stage lasts 5 days with data
 232 input frequency of 6 hours, and the DA window in the EI subsystem is set to 1 day.

233 **2.1.2 Atmospheric transport model**

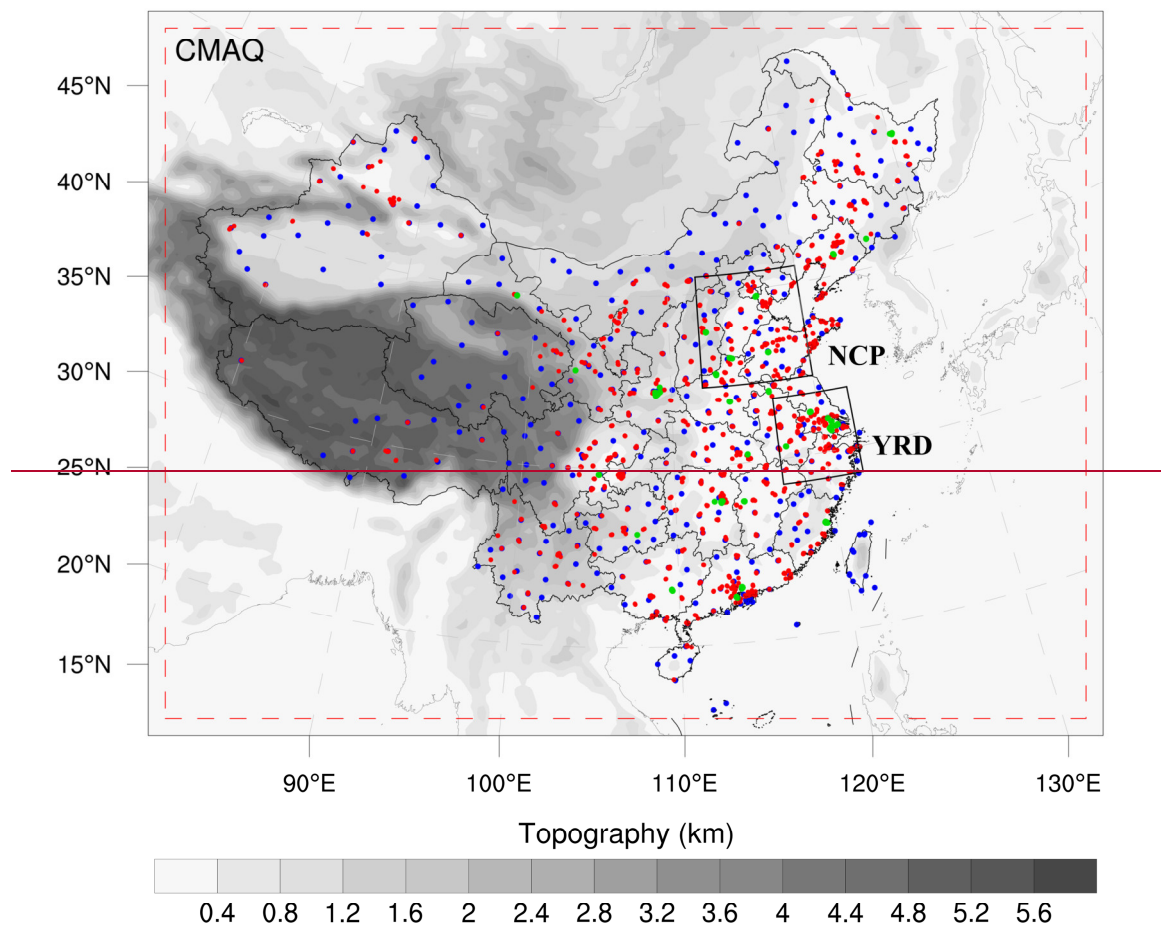
234 The regional chemical transport model of WRF/CMAQ ~~is~~was adopted in this study.
 235 CMAQ is a regional 3-D Eulerian atmospheric chemistry and transport model with a
 236 “one-atmosphere” design developed in the US Environmental Protection Agency (EPA).
 237 It ~~cannot~~ address the complex interactions among multiple pollutants/air quality
 238 issues simultaneously. CMAQ ~~is~~was driven by the WRF model, which is a state of the
 239 art mesoscale numerical weather prediction system designed for both atmospheric
 240 research and meteorological field forecasting. In this study, WRF version 4.0 and
 241 CMAQ version 5.0.2 ~~are~~were adopted. The WRF simulations ~~are~~were performed with
 242 a 36-km horizontal resolution on 169×129 grids, and it covers the whole of mainland
 243 of China (Figure 2). This spatial resolution has been widely adopted in regional

244 simulations and can provide good simulations of the spatiotemporal variations of air
245 pollutants (Mueller and Mallard, 2011; Sharma et al. 2016). In the vertical direction,
246 there are 51 sigma levels on sigma-pressure coordinates extending from the surface to
247 100 hPa. The underlying surface of urban and built-up land ~~is-was~~ replaced by the
248 MODIS land cover retrieval of 2016 to adapt to the rapid expansion of urbanization.
249 The CMAQ model is run with the same domain but with three grid cells removed from
250 each side of the WRF domain. There are 15 layers in the CMAQ vertical coordinate,
251 which ~~are-were interpolated~~~~decompressed~~ from the 51 WRF layers.

252 The meteorological initial and lateral boundary conditions are both provided by the
253 Final (FNL) Operational Global Analysis data of the National Center for Environmental
254 Prediction (NCEP) with a $1^\circ \times 1^\circ$ resolution at 6-h intervals. The chemical lateral
255 boundary conditions and chemical ICs in the IA subsystem come from the background
256 profiles. As mentioned above, in the EI subsystem, the chemical IC in the first window
257 is provided by the IA subsystem, and in the following windows, it is forward simulated
258 using optimized emission ~~from the of~~ previous window. The Carbon Bond 05 with
259 updated toluene chemistry (CB05tucl) and the 6th generation aerosol module (AERO6)
260 are chosen as the gas-phase and aerosol chemical mechanisms, respectively (Appel et
261 al., 2013; Sarwar et al., 2012). Detailed physical and chemical configurations are listed
262 in Table 1.



263



264

265 **Figure 2.** Model domain and observation network. The red dashed frame depicts the
 266 CMAQ computational domain; the ~~blue-dot~~black squares represent the surface
 267 meteorological measurement sites; ~~the turquoise triangles represent the sounding sites;~~
 268 and the red and ~~green-blue~~ dots represent the air pollution measurement sites.
 269 Observations of all sites are assimilated in the 3DVAR subsystem, while observations
 270 of city sites where red dots are averaged are used for assimilation and where green dots
 271 are averaged are used for independent evaluation in EI subsystem; the boxed subregions
 272 are the North China Plain (NCP) and Yangtze River Delta (YRD); and the shaded area
 273 depicts the topography.

274

275

276

277 **Table 1.** Configuration options of WRF/CMAQ

WRF		CMAQ	
Parameter	Scheme	Parameter	Scheme
Microphysics	WSM6	Horizontal/Vertical advection	yamo/wrf
Longwave	RRTM	Horizontal/Vertical diffusion	multiscale/acm2
Shortwave	Goddard	Deposition	m3dry
Boundary layer	ACM	Chemistry solver	EBI
Cumulus	Kain-Fritsch	Photolysis	phot_inline
Land-surface	Noah	Aerosol module	AERO6
Surface layer	Revised	Cloud module	cloud_acm_ae6
Urban canopy	No	Gas-phase chemistry	CB05tucl

278 **2.1.3 3DVAR assimilation algorithm**

279 The Grid-point Statistical Interpolation (GSI) developed in the US National Centers for
 280 Environmental Prediction (NCEP) ~~is~~was employed in this study. Building upon the
 281 work of Liu et al. (2011), Jiang et al. (2013**b**) and Feng et al. (2018), we extended it to
 282 simultaneously assimilate multiple species (including CO, SO₂, NO₂, O₃, PM_{2.5}, and
 283 PM₁₀) and first used individual aerosol species of PM_{2.5} as analysis variables within the
 284 GSI/WRF/CMAQ framework. Additional ~~work includes~~works include the construction
 285 of surface air pollutant observation operators, the updating of observation errors, and
 286 the statistics of background error covariance for the analysis variables. Moreover, the
 287 data interface ~~is~~was also modified to read/write the CMAQ output/input file directly,
 288 which is easy to implement.

289 In the sense of a minimum analysis error variance, the 3DVAR algorithm optimizes
 290 analysis fields with observations by iterative processes to minimize the cost function
 291 (J(x)) defined below:

292
$$J(\mathbf{x}) = \frac{1}{2}(\mathbf{x}_a - \mathbf{x}_b)^T \mathbf{B}^{-1}(\mathbf{x}_a - \mathbf{x}_b) + \frac{1}{2}[H(\mathbf{x}_a) - \mathbf{y}]^T \mathbf{R}^{-1}[H(\mathbf{x}_a) - \mathbf{y}], \quad (1)$$

293 where \mathbf{x}_a is a vector of the analysis field; \mathbf{x}_b denotes the background field; \mathbf{y} is the
 294 vector of observations; \mathbf{B} and \mathbf{R} are the background and observation error covariance
 295 matrices, respectively, representing the relative contributions to analysis; and H is the
 296 observation operator that maps the model variables to the observation space.

297 The analysis variables are the 3D mass concentrations of the pollution compositions
 298 (e.g., CO and sulfate) at each grid point. Hourly mean surface pollution observations
 299 within a 1 hour window of the analysis are assimilated. To assimilate the surface
 300 pollution observations, model-simulated compositions are first diagnosed at the
 301 observation locations. For gas concentrations ~~pollutions~~ that are directly used as
 302 analysis variables, data units need to be converted from ppm or ppb to mg m^{-3} or $\mu\text{g m}^{-3}$
 303 to match with observations. The model-simulated $\text{PM}_{2.5}$ and PM_{10} concentrations at
 304 the ground level are diagnosed as follows:

$$305 \quad PM_{2.5} = f_i \times PM_i + f_j \times PM_j + f_k \times PM_k = \text{OC} + \text{EC} + \text{SO}_4^{2-} + \text{NO}_3^- + \text{NH}_4^+ + \\
 306 \quad \text{SEAS} + \text{AP}_{2.5} \quad (2)$$

$$307 \quad PM_{10} = PM_i + PM_j + PM_k = PM_{2.5} + \text{PMC} \quad (3)$$

308 where f_i , f_j , and f_k are the $\text{PM}_{2.5}$ fractions of the Aitken, accumulation, and coarse
 309 modes, respectively. These ratios are recommended as the concentrations of $\text{PM}_{2.5}$ and
 310 fine mode aerosols (i.e., Aitken plus accumulation) could differ because the $\text{PM}_{2.5}$
 311 particles include small tails from the coarse mode in the CMAQ model (Binkowski and
 312 Roselle, 2003; Jiang et al., 2006). PM_i , PM_j , and PM_k represent the mass
 313 concentrations of the 3 modes in the CMAQ model. Seven aerosol species of $\text{PM}_{2.5}$,
 314 including organic carbon (OC), elemental carbon (EC), sulfate (SO_4^{2-}), nitrate (NO_3^-),
 315 ammonium (NH_4^+), sea salt (SEAS), and fine-mode unspciated aerosols ($\text{AP}_{2.5}$), and
 316 additional coarse PM_{10} (PMC) are extracted as analysis variables, which are updated
 317 by the $\text{PM}_{2.5}$ and PMC observations, respectively. Before the calculation of equation (1)
 318 within the GSI, the analysis variables are bilinearly interpolated in the horizontal
 319 direction to the observation locations.

320 The computation of background error covariance (\mathbf{B}) is generally costly and difficult
 321 when a high-dimensional numerical model is used. For simplification, \mathbf{B} is represented
 322 as a product of spatial correlation matrices and standard deviations (SDs):

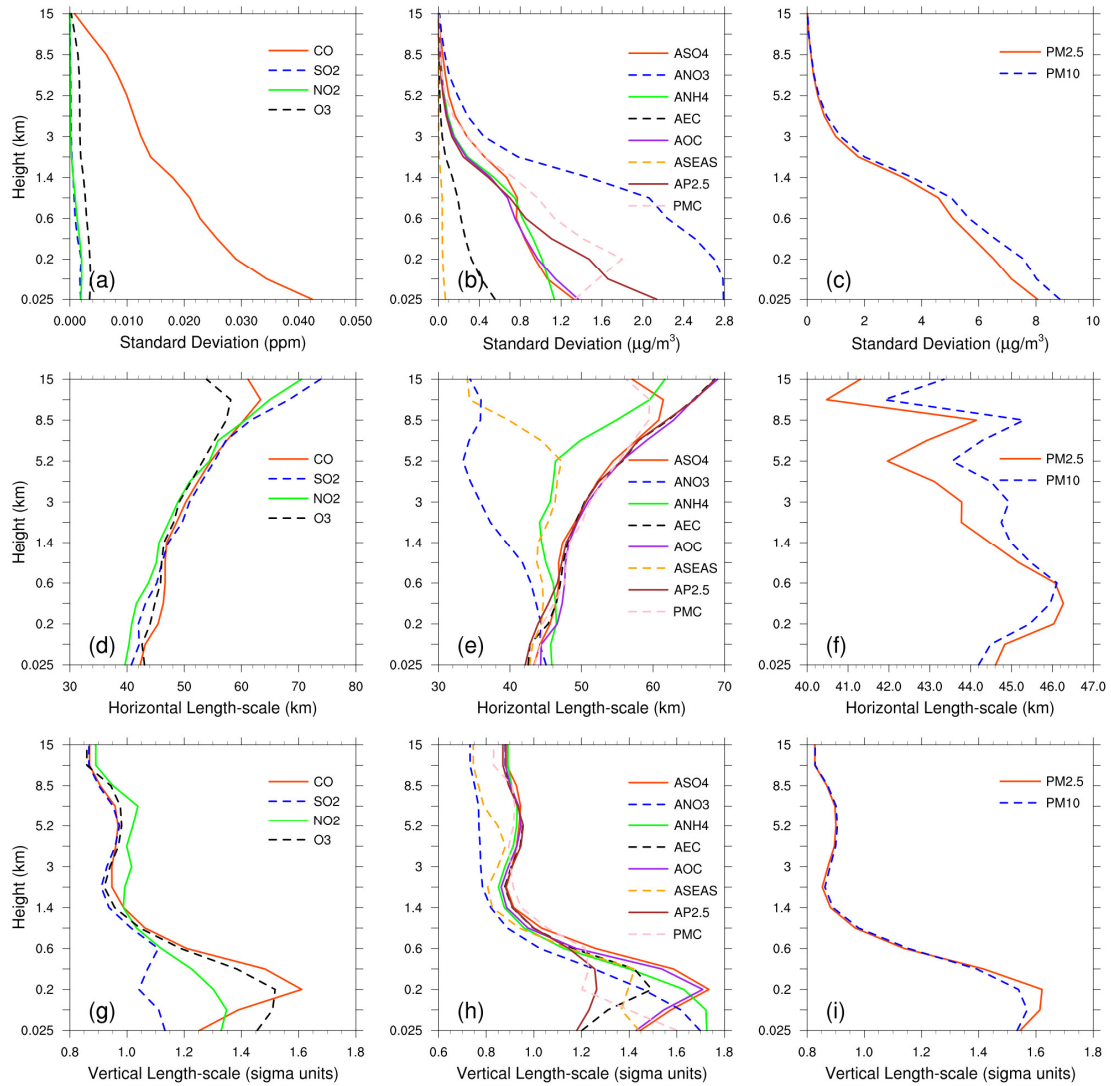
$$323 \quad \mathbf{B} = \mathbf{D}\mathbf{C}\mathbf{D}^T \quad (4)$$

$$324 \quad \mathbf{C} = \mathbf{C}_x \otimes \mathbf{C}_y \otimes \mathbf{C}_z \quad (5)$$

325 where \mathbf{D} is the background error SD matrix, \mathbf{C} is the background error correlation
 326 matrix, \otimes denotes the Kronecker product, and \mathbf{C}_x , \mathbf{C}_y , and \mathbf{C}_z denote three one-
 327 dimensional correlation submatrices in the longitude, latitude, and vertical coordinate
 328 directions, respectively. \mathbf{C}_x and \mathbf{C}_y are assumed to be isotropic horizontally such that
 329 can be represented using a Gaussian function. The correlation between any two points
 330 x_i and x_j in the horizontal can be expressed as follows:

$$331 \quad c(x_i, x_j) = e^{-\frac{(x_i-x_j)^2}{2L^2}} \quad (6)$$

332 where L is the horizontal correlation scale, which is estimated using the proxy of the
 333 background error (Figure 3). The vertical correlation matrix \mathbf{C}_z is directly estimated
 334 from the model background field since \mathbf{C}_z is only an $n_z \times n_z$ (here, $n_z=15$) matrix.



335

336 **Figure 3.** Vertical profiles of standard deviations (top, $\mu\text{g m}^{-3}$), horizontal length scale
 337 (middle, km) and vertical length scale (bottom, km) for CO, SO₂, NO₂, O₃, sulfate,
 338 nitrate, ammonium, EC, OC, sea salt, unspciated aerosols (AP_{2.5}), PMC, PM_{2.5} and
 339 PM₁₀.

340 To estimate these matrices, the “NMC” method is used here to compute **B** for each
 341 variable by taking the differences between forecasts of different lengths valid at the
 342 same time (Parrish and Derber, 1992; Rabier et al., 1998). Differences between 24- and
 343 12-h WRF/CMAQ forecasts of 60 pairs (two pairs a day) of analysis variables valid at
 344 either 0000 or 1200 UTC over November 2016 are used. The horizontal and vertical
 345 length scales of the correlation matrices are estimated by recursive filters (Purser et al.,
 346 2003). The vertical distribution of background error SDs is shown in Figure 3, which

347 varies with height and species. The vertical profile of the background error SDs
348 corresponds to the vertical concentration distribution. This means that higher
349 concentrations tend to have larger background error SDs (e.g., CO and nitrate). These
350 SDs exhibit a common reduction with height, especially at the top of the boundary layer.
351 The horizontal correlation of background error determines the propagation of
352 observation information in this direction, while vertical correlation determines the
353 vertical extension of such increments. For gaseous pollutants and most individual
354 aerosol components, ~~excluding nitrate and sea salt~~, the horizontal length scales ~~decrease~~
355 increase with ~~increasing~~ heights, while for the total particulate matter (i.e., PM_{2.5} and
356 PM₁₀), the scales increase with height ins slightly under the boundary layer and ~~then~~
357 ~~decreases~~ with height slightly over the boundary layer in the free troposphere. The
358 ground-level scale generally spreads 40-45 km for all control variables on average. The
359 vertical length scale of most species increases first and then decreases with height,
360 which may be related to the vertical mixing (Kahnert, 2008) and stack emissions at
361 about 200 m height. ~~The vertical length scale of most species increases with height near~~
362 ~~the ground where they are emitted (Descombes et al., 2015) and then drops rapidly to~~
363 ~~the height of the upper stable atmosphere, with a scale of 1.4 km.~~

364 **2.1.4 EnKF assimilation algorithm**

365 In EnKF, the time-dependent uncertainties of the state variables are estimated using a
366 Monte Carlo approach through an ensemble. Uncertainty can be propagated with linear
367 or nonlinear dynamic models (flow-dependent background error covariance) by simply
368 implementing ensemble simulations. The EnSRF algorithm introduced by Bierman
369 (1977) and Maybeck (1979) (~~Whitaker and Hamill, 2002~~) is used to constrain pollution
370 emissions in this study. EnSRF is a deterministic EnKF that obviates the need to perturb
371 observations, which has a higher computational efficiency and a better performance
372 (Sun et al., 2009).

373 The perturbation of prior emissions represents the uncertainty. We implement additive
374 emission adjustment methods, which are calculated using the following function.

$$375 \quad \mathbf{X}_i^b = \mathbf{X}_0^b + \delta \mathbf{X}_i^b, i = 1, 2, \dots, N \quad (7)$$

376 where \mathbf{b} represents the background (prior) state, i is the identifier of the perturbed
 377 samples, N is the ensemble size, which was set to 40 in consideration of a tradeoff
 378 between the computation cost and inversion accuracy (Figure S1)(40 in this study), and
 379 $\delta \mathbf{X}_i^b$ represents the randomly perturbed samples that are added to the prior emissions
 380 \mathbf{X}_0^b to produce ensemble samples of the inputs \mathbf{X}_i^b . $\delta \mathbf{X}_i^b$ is drawn from Gaussian
 381 distributions with a mean of zero and the standard deviation of the prior emission
 382 uncertainty in each grid. The state variables of the emissions include CO, SO₂, NO_x,
 383 primary PM_{2.5} (PPM_{2.5}) and PMC. We used variable localization to update the analysis,
 384 which means that the covariance among different state variables was not considered,
 385 and the emission of one species was only constrained with its corresponding air
 386 pollutant observation. This method has been widely used in chemical data assimilation
 387 systems to avoid spurious correlations among species. (Ma et al., 2019; Miyazaki et al.,
 388 2012b).is set to zero (Miyazaki et al., 2012b).

389 After obtaining an ensemble of state vectors (prior emissions), ensemble runs of the
 390 CMAQ model are conducted to propagate these errors in the model with each ensemble
 391 sample of state vectors. Combined with observational vector \mathbf{y} , the state vector is
 392 updated by minimizing the analysis variance:

$$393 \quad \overline{\mathbf{X}}^a = \overline{\mathbf{X}}^b + \mathbf{K}(\mathbf{y} - \mathbf{H}\overline{\mathbf{X}}^b) \quad (8)$$

$$394 \quad \mathbf{K} = \mathbf{P}^b \mathbf{H}^T (\mathbf{H} \mathbf{P}^b \mathbf{H}^T + \mathbf{R})^{-1} \quad (9)$$

$$395 \quad \mathbf{P}^b = \frac{1}{N-1} \sum_{i=1}^N (\mathbf{X}_i^b - \overline{\mathbf{X}}^b) (\mathbf{X}_i^b - \overline{\mathbf{X}}^b)^T \quad (10)$$

$$396 \quad \delta \mathbf{X}_i^a = \delta \mathbf{X}_i^b - \tilde{\mathbf{K}} \mathbf{H} \delta \mathbf{X}_i^b \quad (11)$$

397 While employing sequential assimilation and independent observations, $\tilde{\mathbf{K}}$ is
 398 calculated as follows:

$$399 \quad \tilde{\mathbf{K}} = \left(1 + \sqrt{\mathbf{R} / (\mathbf{H} \mathbf{P}^b \mathbf{H}^T + \mathbf{R})} \right)^{-1} \mathbf{K} \quad (12)$$

400 where \bar{X}^b represents the mean of the ensemble samples; H is the observation
 401 operator that maps simulated concentrations from model space to observation space;
 402 $y - H\bar{X}^b$ reflects the differences between the simulated and observed concentrations;
 403 P^b is the ensemble-estimated background (a priori) error covariance; $P^b H^T$ contains
 404 the response of the uncertainty in the simulated concentrations to the uncertainty in
 405 emissions; K is the Kalman gain matrix of the ensemble mean depending on the P^b
 406 and observation error covariance R , representing the relative contributions to analysis;
 407 and \tilde{K} is the Kalman gain matrix of the ensemble perturbation, which is used to
 408 calculate emission perturbations after inversions δX_i^a . The ensemble mean \bar{X}^a of the
 409 analyzed state is taken as the best estimate of the emissions.

410 With large volumes of site observations that are recorded at a much higher resolution
 411 than the model grid spacing, there would be significant correlated or fully consistent
 412 model-data mismatch errors in one cluster, resulting in excessive adjustments and
 413 deteriorated model performances (Houtekamer and Mitchell, 2001). To reduce the
 414 horizontal observation error correlations and the influence of representativeness errors,
 415 a “super-observation” approach combining multiple noisy observations located within
 416 the same grid and assimilation window is developed based on optimal estimation theory
 417 (Miyazaki et al., 2012a). Previous studies have demonstrated the necessity of data-
 418 thinning and dealiasing errors (Feng et al., 2020b; Zhang et al., 2009a). The super-
 419 observation y_{new} , super-observation error r_{new} and corresponding simulation $x_{new,i}$
 420 of the i th sample are calculated as follows:

$$421 \quad 1/r_{new}^2 = \sum_{j=1}^m 1/r_j^2 \quad (13)$$

$$422 \quad y_{new} = \sum_{j=1}^m w_j y_j / \sum_{j=1}^m w_j \quad (14)$$

$$423 \quad x_{new,i} = \sum_{j=1}^m w_j x_{ij} / \sum_{j=1}^m w_j \quad (15)$$

424 where j is the identifier of m observations within a super-observation grid; r_j is the
 425 observational error of actual j th observation y_j ; x_{ij} represents a simulated

426 concentration using the i th prior emission sample corresponding to the j th observation;
427 and $w_j = 1/r_j^2$ is the weighting factor. The super-observation error decreases as the
428 number of observations used within a super-observation increases. This method has
429 been used in our previous inversions using surface-based (Feng et al., 2020b) and
430 satellite-based (Jiang et al., 2021) observations.

431 In this study, the DA window ~~is~~was set to 1 day because the model needs a longer time
432 to integrate emission information into the concentration ensembles (Ma et al., 2019).
433 Due to the “super-observation” approach, only one assimilation is needed in one
434 assimilation window. In addition, due to the complexity of hourly emissions, it is very
435 difficult to simulate hourly concentrations that can match the observations well.
436 Although a longer DA window could allow more observations to constrain the emission
437 change of one grid, the spurious correlation signals of EnKF would attenuate
438 observation information with time (Bruhwiler et al., 2005; Jiang et al., 2021). Kang et
439 al. (2012) conducted OSSEs and demonstrated that due to the errors of transport and
440 increase the spurious correlation, a longer DA window (e.g., 3 weeks) would cause the
441 analysis system to blur out the essential emission information far away from the
442 observation. Kang et al. (2012) and Zhang et al. (2015) also pointed out that the emission
443 inversion with a long window (e.g., 1 to 3 weeks) is not as accurate as that obtained
444 with a short DA window (e.g., 6 hours to 1 week). Therefore, daily mean simulations
445 and observations are used in the EnSRF algorithm, and daily emissions are optimized
446 in this system. _

447 EnKF is subject to spurious correlations due to the limited number of ensembles when
448 it is applied in high-dimensional atmospheric models, which can cause rank
449 deficiencies in the estimated background error covariance and filter divergence, and
450 further degrade analyses and forecasts (Wang et al., 2020). Covariance localization is
451 performed to reduce spurious correlations caused by the finite ensemble size
452 (Houtekamer and Mitchell, 2001). Covariance localization preserves the meaningful

453 impact of observations on state variables within a certain distance (cutoff radius) but
454 limits the detrimental impact of observations on remote state variables. The localization
455 function of Gaspari and Cohn function (Gaspari and Cohn, 1999) is used in this system,
456 which is a piecewise continuous fifth-order polynomial approximation of a normal
457 distribution. The optimal localization scale is related to the ensemble size, assimilation
458 window, dynamic system, and lifetime of a chemical species in the atmosphere. CO,
459 SO₂ and PM_{2.5} are rather stable in atmosphere, with a lifetime more than 1 day.
460 According to the averaged wind speed (3.3 m/s, Table 4) and the length of DA window,
461 their localization scales are set to 300 km. In addition, NO₂ is rather ~~reactive~~active, with
462 a lifetime of approximately 10 hours in winter (de Foy et al., 2015), and PMC, which
463 is mainly from local sources, its residence time in the atmosphere is also short due to
464 the rapid deposition rate (Clements et al., 2014; Clements et al., 2016; Hinds, 1982).
465 Their localization scales are set to 150 km and 250 km, respectively.

466 **2.2 Prior emissions and uncertainties**

467 The anthropogenic emissions over China ~~are~~were taken from the 2016 Multi-resolution
468 Emission Inventory for China (MEIC 2016) (Zheng et al., 2018), while those over the
469 other regions of East Asia ~~are~~were obtained from the mosaic Asian anthropogenic
470 emission inventory (MIX) (Li et al., 2017). The spatial resolutions of both the MEIC
471 and MIX inventories are 0.25° × 0.25°, and they are both downscaled to match the
472 model grid spacing of 36 km~~(36 km)~~. The spatial distributions of the CO, SO₂, NO_x,
473 PPM_{2.5} and PMC emissions are shown in Figure ~~12~~0. The daily emission inventory,
474 which ~~is~~was arithmetic averaged from the combined monthly emission inventory, ~~is~~
475 was directly used in the EI subsystem and employed as the prior emission of the first
476 DA window in the EI subsystem (Figure 1). During the simulations, the daily emissions
477 were further converted to hourly emissions. For all the species emitted from area
478 sources, we converted them to hourly using a same diurnal profile (Figure S2), and for
479 the point source, we assumed that there was no diurnal change. MEIC 2012 ~~is~~was used
480 as an alternative a priori over China to investigate the impact of different prior
481 emissions on the optimized emissions. The Model of Emissions of Gases and Aerosols

482 from Nature (MEGAN) (Guenther et al., 2012) ~~is-was~~ used to calculate time-dependent
483 biogenic emissions. It ~~is-was~~ also driven by the WRF model in this study. Biomass
484 burning emissions ~~are-were~~ not included because they have little impact across China
485 during the study period (Zhang et al., 2020).

486 During the ~~inversion cycle~~~~eyeling~~ ~~inversions~~, the inverted emissions of different
487 members converge gradually, and the ensemble-estimated error covariance matrix is
488 ~~arithmetically~~~~very~~ likely to be underestimated. To avoid this, considering the
489 compensation of model errors and comparable emission uncertainties from one day to
490 the next, we impose the same uncertainty on emissions at each DA window. As
491 mentioned above, the optimized emissions of the current DA window are transferred to
492 the next DA window as prior emissions. The technology-based emission inventory
493 developed by Zhang et al. (2009b), basically using the same method as MEIC, shows
494 that the emissions of PMC and PPM_{2.5} have the largest uncertainties, followed by CO,
495 and finally SO₂ and NO_x. Therefore, the uncertainties in this study are set to 40%, 40%,
496 30%, 25%, and 25%. However, previous studies have shown that the inversely
497 estimated CO and PMC emissions could exceed 100% higher than the bottom-up
498 emissions (MEIC) in certain areas (Feng et al., 2020b; Ma et al., 2019). According to
499 the extent of underestimation, we set an uncertainty of 100% for both the CO and PMC
500 emissions at the beginning of the three DA windows to quickly converge the emissions.
501 The mean emission analysis is generally minimally sensitive to the uncertainty setting
502 in our ~~assimilation cycle~~~~cycle~~ ~~assimilation~~ method (Feng et al., 2020; Gurney et al.,
503 2004; Miyazaki et al., 2012a) because the inversion errors of the current window could
504 be transferred to the next window for further optimization (Sect. 4.3).

505 **2.3 Observation data and errors**

506 Hourly averaged surface CO, SO₂, NO₂, O₃, PM_{2.5} and PM₁₀ observations from 1504
507 national control air quality stations ~~are-were~~ assimilated in this system, which were
508 obtained from the Ministry of Ecology and Environment of the People's Republic of
509 China (<http://106.37.208.233:20035/>, last access: 25 June 2020). These sites ~~are~~
510 ~~distributed~~~~distribute~~—over most of central and eastern China and become denser near

511 metropolitan areas (see Figure 2). Value-range and time-continuity checks ~~are-were~~
512 performed to ensure data quality. Value-range checks ~~are-were~~ mainly performed to
513 eliminate unrealistic or ~~unrepresentative nonspatially representative~~ observations. Only
514 observations within the subjectively selected threshold range ~~are-were~~ assimilated
515 (Table 2). A time-continuity check ~~is-was~~ performed to eliminate gross outliers and a
516 sudden anomaly using a function of $\max(|O(t) - O(t \pm 1)|) \leq f(t) + O(t) - O(t \pm$
517 $1) \leq f(t)$, where $O(t)$ and $O(t \pm 1)$ represent observations at time t and $t \pm$
518 1 , respectively, and $f(t) = T_a + T_b \times O_t$. ~~That means that both concentration~~
519 ~~differences between time t and time $t+1$ and $t-1$ should be less than $f(t)$.~~ T_b is fixed
520 to 0.15, and the section of T_a is given in Table 2, which is determined empirically
521 according to the time series change of concentration at each site. It should be noted that,
522 to avoid potential cross-correlations, we assimilated $\text{PM}_{2.5}$ and PMC . Additionally, in
523 the EI subsystem, the observations within each city ~~are-were~~ averaged to thin the data
524 density ~~and~~, reduce the error correlation ~~and increase the spatial representation~~
525 (Houtekamer and Mitchell, 2001; Houtekamer and Zhang, 2016). Finally, 336 city sites
526 are available across the mainland of China, in which 311 cities' data ~~are-were~~ selected
527 for assimilation and the remaining 25 ~~are-were~~ selected for independent validation
528 (Figure 2). In the IA subsystem, due to the small horizontal correlation scale (Figure 3),
529 to obtain more extensive observation constraints, all site observations ~~are-were~~
530 assimilated to provide ~~a good~~ "perfect" IC for the next emission inversion.

531 The observation error covariance matrix (\mathbf{R}) includes both measurement and
532 representation errors. The measurement error ε_0 is defined as follow:

$$533 \quad \varepsilon_0 = ermax + ermin \times \Pi_0 \quad (16)$$

534 where $ermax$ is a base error, and Π_0 denotes the observed concentration. These
535 parameters for different species are listed in Table 2, which are determined according
536 to Chen et al. (2019), Feng et al., (2018) and Jiang et al. (2013b).

537 The representative error depends on the model resolution and the characteristics of the
538 observation locations, which ~~is-were~~ calculated using the equations of Elbern et al.

539 (2007) defined as follows:

$$540 \quad \varepsilon_r = \gamma \varepsilon_0 \sqrt{\Delta l / L} \quad (17)$$

541 where γ is a tunable parameter (here, $\gamma=0.5$), Δl is the grid spacing (36 km), and L
542 indicates the radius (here, 3 km for simplification) of influence area of an observation.

543 The total observation error (r) is defined as follows:

$$544 \quad r = \sqrt{\varepsilon_0^2 + \varepsilon_r^2} \quad (18)$$

545 **Table 2.** Parameters of quality control and measurement error

Parameter	CO mg m ⁻³	SO ₂ μg m ⁻³	NO ₂ μg m ⁻³	O ₃ μg m ⁻³	PM _{2.5} μg m ⁻³	PMC μg m ⁻³
value-range	0.1-12	1-800	1-250	1-250	1-800	1-900
time-continuity (T_a)	2.5	160	70	80	180	180
ermax	0.05	1	1	1	1.5	1.5
ermin	0.5%	0.5%	0.5%	0.5%	0.75%	0.75%

546

547 **3 Experimental design**

548 RAPAS ~~is was~~ conducted according to the procedure and settings described in Sect. 2.
549 December is one of the months with most severe air pollution, while July is one of the
550 least polluted months in China. Therefore, this study mainly tested the performance of
551 the RAPAS system in these two months. For December, tThe IA subsystem ~~is was~~ run
552 from 26 to 31 November 2016 with a 6-hour interval cycling assimilation to optimize
553 ICs (ICDA). A better IC at 0000 UTC on December 1 can be obtained by 5-day high-
554 frequency cycling assimilation and atmospheric mixing. Then the EI subsystem ~~is was~~
555 run for December 2016 with a 1-day assimilation window to optimize emissions
556 (EMDA). For July, the system also operated in the same way as for December. It needs
557 to be noted that due to the stronger atmospheric oxidation, the lifetime of NO₂ in July

558 is significantly shorter than that in December, thus we adopted a smaller localization
559 scale for NO₂ (80 km). Both assimilation experiments use the combined prior emission
560 inventories of 2016 as described in Sect. 2.2, and the emission base year coincides with
561 the research stage. An Observing Systems Simulation Experiment (OSSE) was
562 conducted to evaluate the performance of the RAPAS system, which has been widely
563 used in previous assimilation systems development (Daley, 1997). In the OSSE
564 experiment, we used the MEIC 2016 inventory as a “true” emission, and reduced the
565 “true” emission by 30% over the mainland of China as a prior emission. The simulations
566 simulated using the “true” emission and sampled according to the locations and times
567 of the real observations were used as artificial observations. The observation errors are
568 the same as those in EMDA. To evaluate the $_IC$ improvements from the IA subsystem,
569 an experiment without 3DVAR (~~NODAICNO~~) is conducted with the same
570 meteorological fields and physical and chemistry parameterization settings as those of
571 the ICDA. To evaluate the posterior emissions of the EI subsystem, two parallel forward
572 modeling experiments are performed for December 2016, namely, a control experiment
573 (CEP) with prior (MEIC 2016) emissions and a validation experiment (VEP) with
574 posterior emissions. Both experiments use the same initial field at 0000 UTC on
575 December 01 generated through the IA subsystem. Similar to the above, the only
576 differences between CEP and VEP are emissions. Table 3 gives a summary of different
577 emission inversion experiments conducted in this study.~~Table 3 gives a summary of~~
578 ~~these different simulation experiments.~~

579 To investigate the robustness of our system, ~~87~~ sensitivity tests (from EMS1 to EMS~~87~~,
580 see Table 3) are performed. These experiments are all based on EMDA. In EMS1, rather
581 than forward simulated using the optimized emissions of the previous DA window in
582 EMDA, the initial fields of each DA window were first taken from forward simulation
583 with the prior emissions of the previous DA window, and then optimized using the
584 3DVAR algorithm~~the initial fields of each DA window are optimized using the 3DVAR~~
585 ~~algorithm directly~~ and the observations at the corresponding moment as mentioned in
586 Sect. 2.3. The objective of this experiment is to investigate the advantages of the “two-

587 step” calculation scheme in the EI subsystem as introduced in Sect. 2.1. EMS2 uses
588 MEIC 2012 as the original prior emission in China, aiming to investigate the impact of
589 different prior inventories on the estimates of emissions. Four other experiments,
590 namely EMS3-6, aim to test the impact of different prior uncertainty settings, in which,
591 the prior uncertainties are reduced by -50% and -25%, and increased by 25% and 50%,
592 respectively. EMS7 aims to evaluate the impact of observation errors on emission
593 estimates, in which all the observation errors are magnified twice. The last EMS8
594 experiment aims to evaluate the impact of IC optimization of the first window on
595 emission estimates, in which the ICs were taken from a 5-day spin-up simulation. Eight
596 ~~Seven~~ forward modeling experiments (VEP1, VEP2, ..., VEP~~8~~7) ~~are~~ were also
597 performed with posterior emissions of EMS1 to EMS~~8~~7 to evaluate their performances,
598 respectively. _

599

600

601

602

603

604

605

606

607

608

609

610

611

612

Table 3. Emission inversion and sensitivity eExperiments conducted in this study

Exp. Type	Exp. Name	Period	<u>IC of the first DA Window Initial field</u>	<u>ICs of the subsequent DA window</u>	Emission
<u>Assimilation</u>	EMDA	1-31 December	0000 UTC on December 1, taken from ICDA	<u>Forecast with posterior emissions in the previous window</u>	MEIC 2016 for December (the first DA window), optimized emissions of the previous window (other DA windows)
	<u>OSSE</u>	<u>1-31 December</u>	<u>The same as EMDA</u>	<u>The same as EMDA</u>	<u>The same as EMDA, but with a decrease of 30% for CO, SO₂, NO_x, PPM_{2.5}, and PMC</u>
	EMS1	1-31 December	<u>The same as EMDA Forecast with prior emissions in the previous window</u>	<u>Forecast with prior emissions in the previous window and 3DVAR assimilation</u>	The same as EMDA
	EMS2	1-31 December	The same as EMDA	<u>The same as EMDA</u>	The same as EMDA, but for EMIC 2012
Sensitivity	EMS3-6	1-31 December	The same as EMDA	<u>The same as EMDA</u>	The same as EMDA, but with a $\pm 25\%$ or $\pm 50\%$ of default uncertainty
	EMS7	1-31 December	The same as EMDA	<u>The same as EMDA</u>	The same as EMDA, but with a +100% of default observation errors
	<u>EMS8</u>	<u>1-31 December</u>	<u>0000 UTC on December 1, taken from ICNO</u>	<u>The same as EMDA</u>	<u>The same as EMDA</u>

613

614

615 **4 Results**

616 **4.1 Evaluations**

617 **4.1.1 Simulated meteorological fields**

618 In the RAPAS system, the inversion approach attributes all the biases between the
619 simulated and observed concentrations to the emissions. The meteorological fields
620 dominate the physical and chemical processes of the air pollutants in the atmosphere,
621 and thus their simulation accuracy would significantly affect the estimates of emissions
622 in this study. To quantitatively evaluate the performance of the WRF simulations, the
623 mean bias (BIAS), root mean square error (RMSE), and correlation coefficient (CORR)
624 were calculated against the surface meteorological observations measured at 400
625 stations and the planetary boundary layer height (PBLH) calculated using the sounding
626 data at 92 sites. ~~The surface observations~~ which were obtained from the National
627 Climate Data Center (NCDC) integrated surface database
628 (<http://www.ncdc.noaa.gov/oa/ncdc.html>, last access: 25 October 2021), and the
629 sounding data were obtained from the website of the University of Wyoming
630 (<http://weather.uwyo.edu/upperair/sounding.html>, last access: 10 March 2022). The
631 sounding data are in 12 hours interval. The observed PBLH were calculated using the
632 sound data through the bulk Richardson number method (Richardson et al., 2013). The
633 spatial distribution of the meteorological stations ~~(blue dots)~~ is shown in Figure 2. The
634 simulated temperature at 2 m (T2), relative humidity at 2 m (RH2), ~~and~~ wind speed at
635 10 m (WS10), and PBLH from 26 November to 31 December 2016 are evaluated
636 against the observations. Table 4 summarizes the statistical results of the evaluations of
637 the simulated meteorological parameters. Overall, the T2, RH2 and PBLH are slightly
638 underestimated, with biases of -0.1 °C, -3.8% and -41.1 m, respectively. The CORRs
639 are approximately 0.98 for T2, 0.94 for RH2 and 0.90 for PBLH. ~~Overall, the T2 and~~
640 ~~RH2 are slightly underestimated, with biases of -0.1 °C and -3.8%, respectively. The~~
641 ~~CORRs are approximately 0.98 for T2 and 0.94 for RH2,~~ showing good consistency
642 between the observations and simulations. The WS10 is overestimated, with a bias of

643 0.7 m/s and an RMSE of 0.8 m/s, but is better than many other studies (Chen et al.,
 644 2016; Jiang et al., 2012a; Jiang et al., 2012b). Therefore, WRF can generally reproduce
 645 the meteorological conditions sufficiently in terms of their temporal variation and
 646 magnitude over China, which is adequate for our inversion estimation.

647 **Table 4.** Statistics comparing the simulated and observed 10-m wind speed (WS10,
 648 ~~m/s~~), 2-m temperature (T2,~~°C~~), and 2-m relative humidity (RH2,~~%~~), and planetary
 649 boundary layer height (PBLH). averaged over all 400 stations.

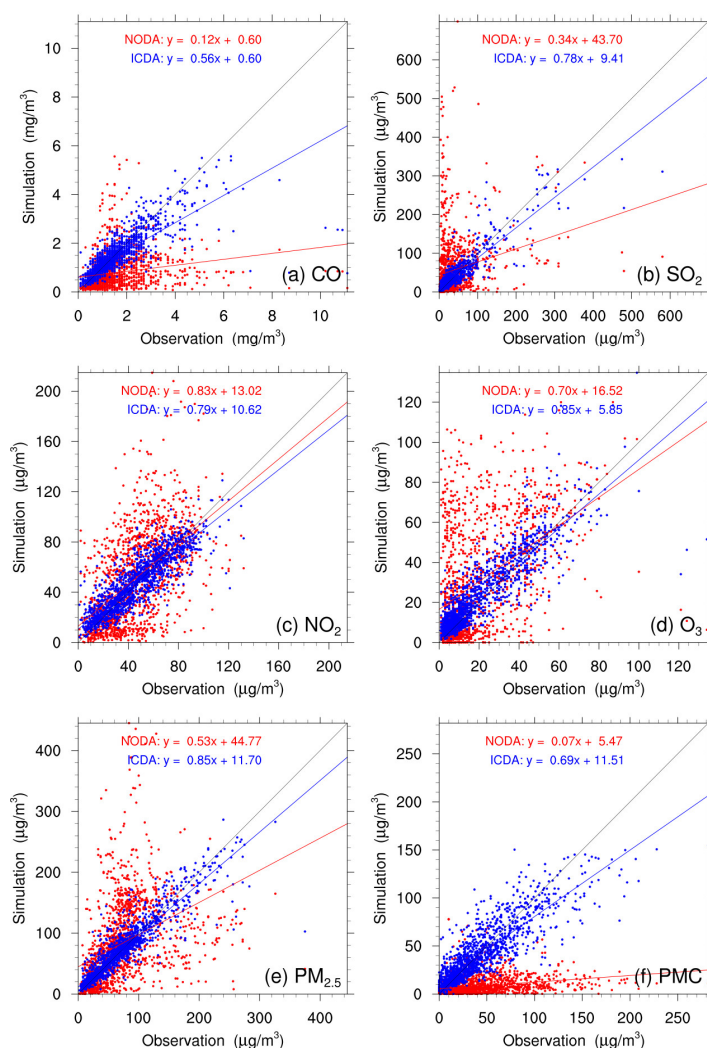
Variable Met.	<u>No. of sites</u>	Mean Obs.	Mean Sim.	BIAS	RMSE	CORR
WS10 (m/s)	<u>400</u>	2.6	3.3	0.7	0.8	0.72
T2 (°C)	<u>400</u>	2.9	2.8	-0.1	0.7	0.98
RH2 (%)	<u>400</u>	66.3	62.6	-3.8	5.2	0.94
<u>PBLH (m)</u>	<u>92</u>	<u>267.5</u>	<u>226.4</u>	<u>-41.1</u>	<u>50.4</u>	<u>0.90</u>

650 * BIAS, mean bias; RMSE, root mean square error; CORR, correlation coefficient

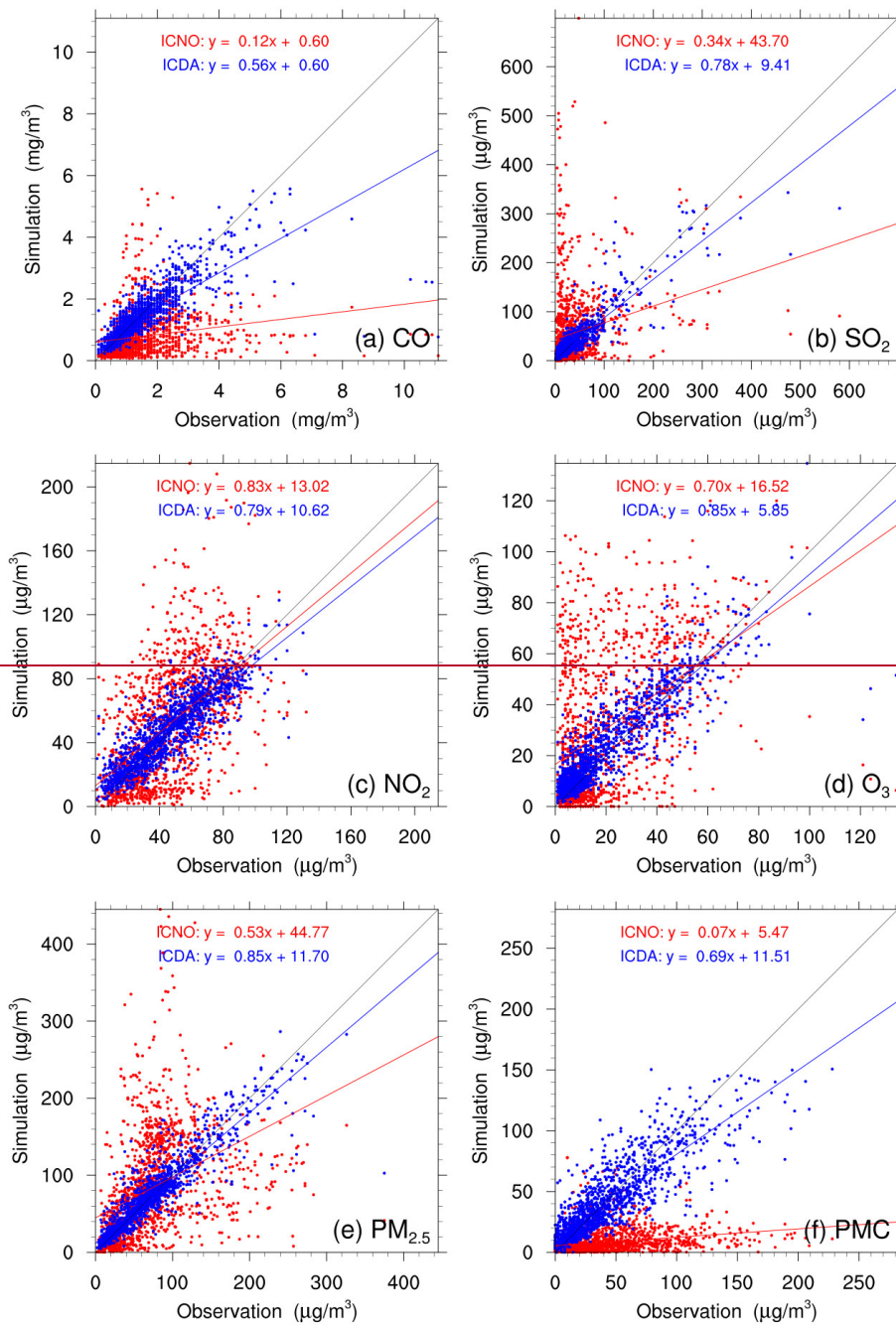
651 **4.1.22 Initial fields**

652 Figure 4 shows the evaluations of the analyzed concentrations of the 6 species against
 653 surface observations. For comparison, the evaluations of the simulations without
 654 3DVAR (~~NODAI_{ICNO}~~) are also shown in Figure 4. The simulations of the
 655 ~~NODAI_{ICNO}~~ experiment (red dots) are scattered on both sides of a central line, as large
 656 systematic biases remain across many measurement sites. Conversely, the ICDA
 657 experiment (blue dots) shows much better agreement with observations than those from
 658 ~~NODAI_{ICNO}~~. The statistics show that there are large systematic biases in the
 659 ~~NODAI_{ICNO}~~ simulations, with large RMSEs and small CORRs for all species,
 660 especially for CO and PMC. After the assimilation of surface observations, the RMSE
 661 of CO decreases to 0.7 mg m⁻³, and those of SO₂, NO₂, O₃, PM_{2.5} and PMC decrease to
 662 22.0, 12.0, 9.6, 20.5 and 19.6 μg m⁻³, respectively, with respective reduction rates of
 663 50.0%, 73.1%, 61.0%, 64.7%, 69.5%, and 60.8% compared to the ones of the
 664 ~~NODAI_{ICNO}~~ (Table 5). The CORRs of ICDA increase by 290.0%, 291.3%, 55.4%,

665 87.2%, 130.0% and 214.8% to 0.78, 0.90, 0.87, 0.88, 0.92 and 0.85, respectively. These
 666 statistics indicate the initial fields of the ground level have been significantly improved.
 667 However, due to the lack of observations, we still do not know the simulation bias in
 668 the upper-middle boundary layer. Although concentrations at high altitudes can be
 669 constrained by ground-based observations through vertical correlations, the effect is
 670 limited, so the bias is still non-negligible.~~that the initial fields can be adjusted~~
 671 ~~effectively by our IA subsystem.~~



672



673

674 **Figure 4.** Scatter plots of simulated versus observed (a) CO, (b) SO₂, (c) NO₂, (d) O₃,
 675 (e) PM_{2.5} and (f) PMC mass concentrations at 0000 UTC on December 1 initializations
 676 from the background (red) and analysis (blue) fields.

677

678

679 **Table 5.** Comparisons of the surface CO, SO₂, NO₂, O₃, PM_{2.5} and PMC mass
 680 concentrations from the control and assimilation experiment against observations
 681 aggregated over all analysis times. CO unit: mg m⁻³; others units: µg m⁻³.

Species	Exp. Name	Mean Obs.	Mean Sim.	BIAS	RMSE	CORR
CO	NODAIENØ	1.5	0.8	-0.7	1.4	0.20
	ICDA		1.5	-0.1	0.7	0.78
SO ₂	NODAIENØ	36.3	56.0	19.7	81.7	0.23
	ICDA		37.8	1.5	22.0	0.90
NO ₂	NODAIENØ	45.8	51.1	5.3	30.8	0.56
	ICDA		47.0	1.1	12.0	0.87
O ₃	NODAIENØ	20.5	30.8	10.4	27.2	0.47
	ICDA		23.3	2.8	9.6	0.88
PM _{2.5}	NODAIENØ	70.9	82.2	11.3	67.3	0.40
	ICDA		71.8	0.9	20.5	0.92
PMC	NODAIENØ	43.5	8.5	-35.0	50.0	0.27
	ICDA		41.6	-1.9	19.6	0.85

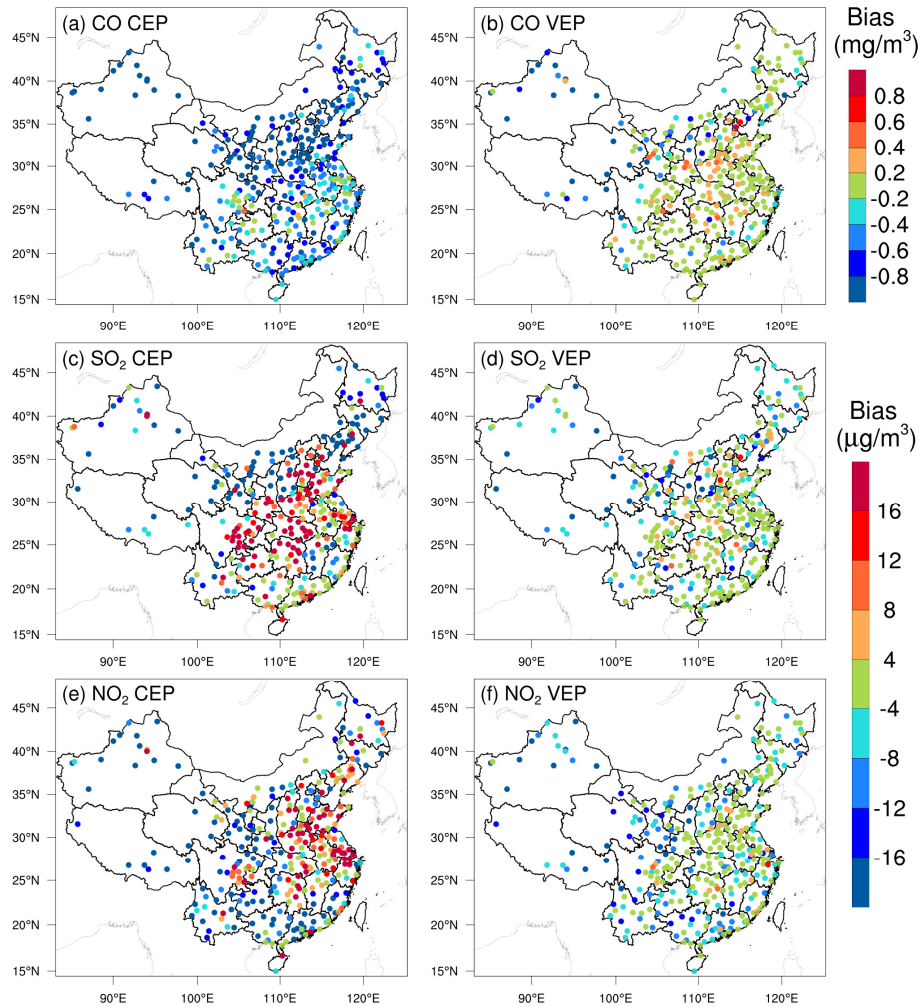
682 * BIAS, mean bias; RMSE, root mean square error; CORR, correlation coefficient

683 4.1.3 Posterior emissions

684 Due to mismatched spatial scales, it is difficult to directly evaluate the optimized
 685 emissions against observations. Generally, we indirectly validate them by comparing
 686 the forward simulated concentrations using the posterior emissions against atmospheric
 687 measurements (e.g., Jiang et al. (2014), Jin et al. (2018), and Peters et al. (2007)). Figure
 688 5 shows the spatial distributions of the mean biases between the simulated gaseous
 689 pollutants using prior and posterior emissions and assimilated observations. In the CEPs,
 690 for each species, the distribution of biases is similar to the increments in background
 691 fields constrained through 3DVAR as shown in Figure S3. For example, almost all sites
 692 have large negative biases for CO, while for SO₂ and NO₂, positive biases are mainly
 693 distributed over the North China Plain (NCP), Yangtze River Delta (YRD), Sichuan
 694 Basin (SCB) and Central China, and negative biases are over the rest of the areas. After
 695 constraining with observations, the biases of all the 3 gaseous air pollutants are

696 significantly reduced in most sites. For CO, the biases at 62% of the sites decreased to
697 absolute values less than 0.2 mg m^{-3} , and for SO₂ and NO₂, the biases at 52% and 47%
698 of the sites were within $\pm 4 \text{ } \mu\text{g m}^{-3}$. However, large negative biases are still observed in
699 part of western Chinas, indicating that the uncertainties of the posterior emissions are
700 still large in western China, which may be attributed to the large biases in prior
701 emissions and to the relatively limited observation. Overall, the statistics show that
702 there are different levels of improvements at 92%, 85% and 85% of the total 311
703 assimilation sites for CO, SO₂ and NO₂, respectively. The small amount of sites with
704 worse performance may be related to the overadjusted emissions by EI or contradictory
705 adjustments caused by opposite biases in adjacent areas.

706 Table 6 lists the statistical results of the evaluations averaged over the whole mainland
707 of China. For CO, the mean bias is -0.8 mg m^{-3} with the prior emissions, while it
708 substantially reduces to -0.1 mg m^{-3} with a reduction rate of 89.6% when simulating
709 with the posterior emissions. Additionally, the RMSE decreases by 48.1% from 1.08 to
710 0.56 mg m^{-3} , and the CORR increases by 76.1% from 0.46 to 0.81. For SO₂ and NO₂,
711 the regional mean biases slightly increase as the positive/negative biases among
712 different sites might be offset. However, the RMSEs decrease to 17.7 and $12.3 \text{ } \mu\text{g m}^{-3}$,
713 respectively, which are 58.3% and 50.8% lower than those of CEPs, and the CORRs
714 increase by 125.6% and 35.4%, both reaching up to 0.88, indicating that EI has
715 significantly improved the NO_x and SO₂ emission estimates.

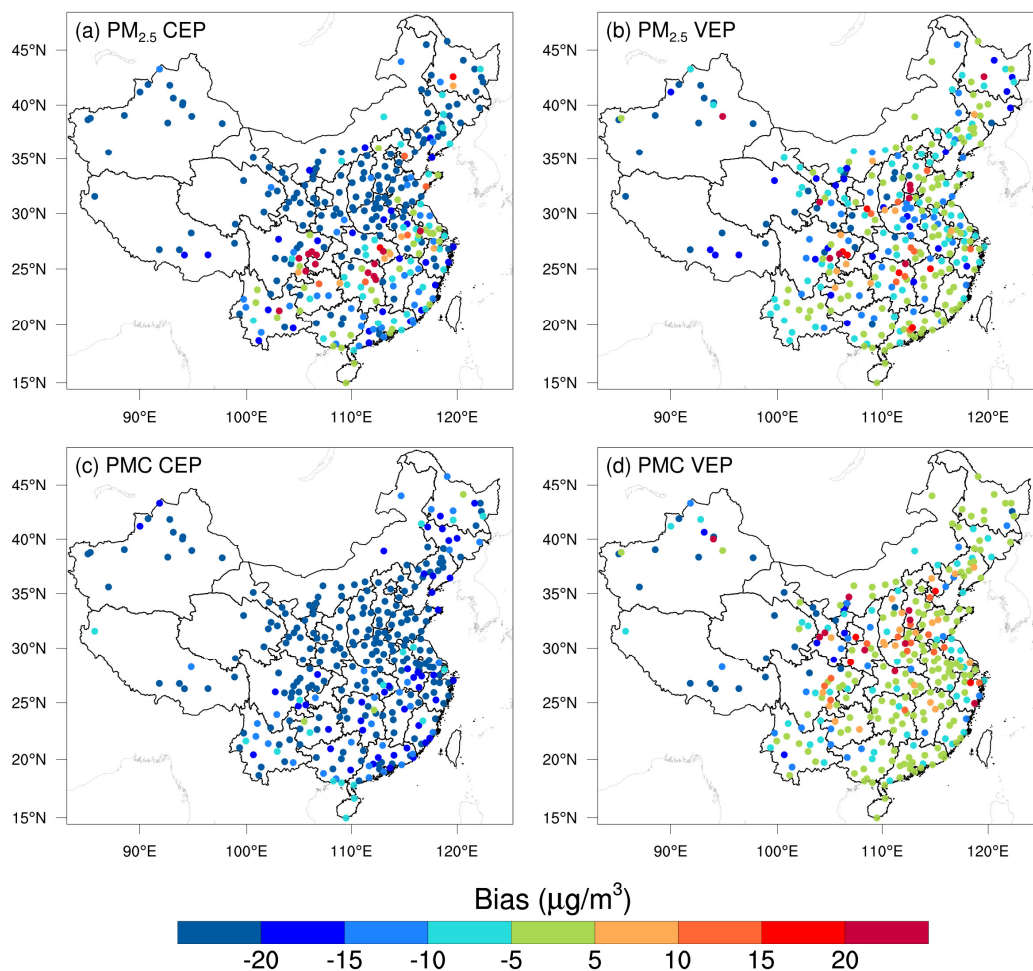


716

717 **Figure 5.** Spatial distribution of the BIAS of the simulated (a, b) CO, (c, d) SO₂ and (e,
 718 f) NO₂ with prior (left, CEP) and posterior (right, VEP) emissions. CO unit: mg m⁻³;
 719 SO₂ and NO₂ units: µg m⁻³.

720 Figure 6 shows the spatial distributions of the mean biases of simulated PM_{2.5} and PMC
 721 evaluated against the assimilated observations. Similarly, the CEP simulations do not
 722 perform well. There are widespread underestimations across the country, with mean
 723 biases of -24.0 and -32.4 µg m⁻³. After data assimilation, the performance of VEP
 724 simulations is significantly improved. The biases decrease by 72.1% and 90.4% to -6.7
 725 and -3.1 µg m⁻³, the RMSEs decrease by 41.2% and 40.7% to 29.6 and 24.6 µg m⁻³, and
 726 the CORRs increase by 35.9% and 176.0% to 0.87 and 0.69 for PM_{2.5} and PMC,
 727 respectively. Overall, 89.6% and 97.2% of the assimilation sites are improved for PM_{2.5}

728 and PMC, respectively. However, compared with the results of the 3 gaseous pollutants,
729 there are sites with large biases scattered throughout the whole domain. Besides the
730 potential overadjusted or contradictory adjustments of emissions as in the 3 gas species,
731 It may also be related to the complex precursors and complex homogeneous and
732 heterogeneous chemical reactions and transformation processes of secondary PM_{2.5}†
733 ~~may be also related to the complex precursors and the nonlinear responses to its~~
734 ~~precursors for PM_{2.5},~~ and the fact that we do not simulate the time variation of dust
735 blowing caused by wind speed for PMC due to the lack of land cover data that is
736 compatible with the CMAQ dust module and agricultural activities data to identify dust
737 source regions.

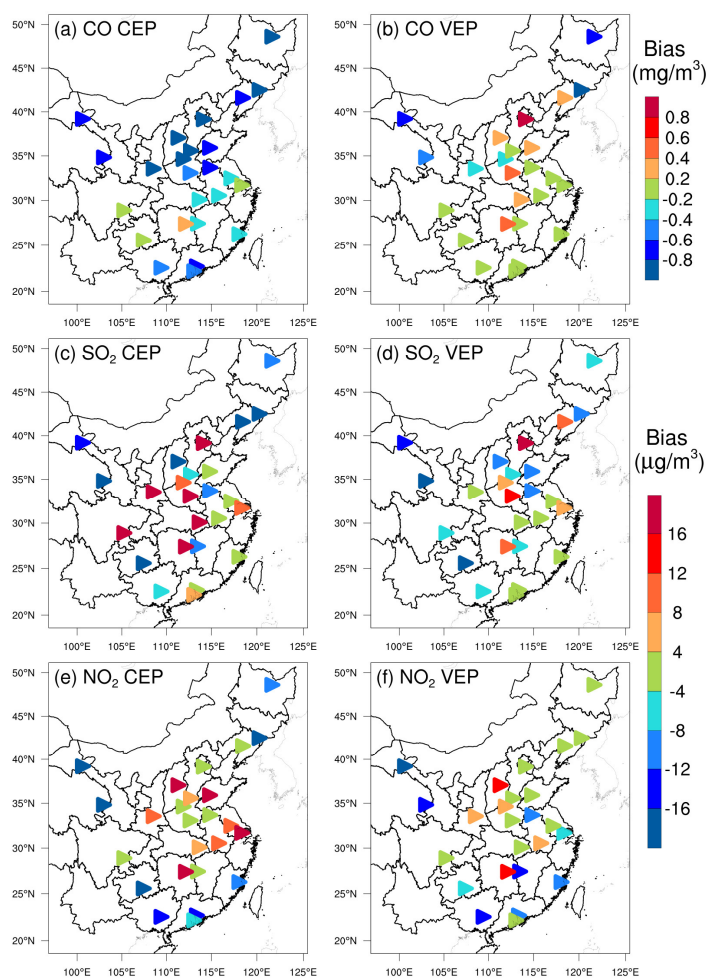


738

739

Figure 6. Same as in Figure 5 but for PM_{2.5} and PMC.

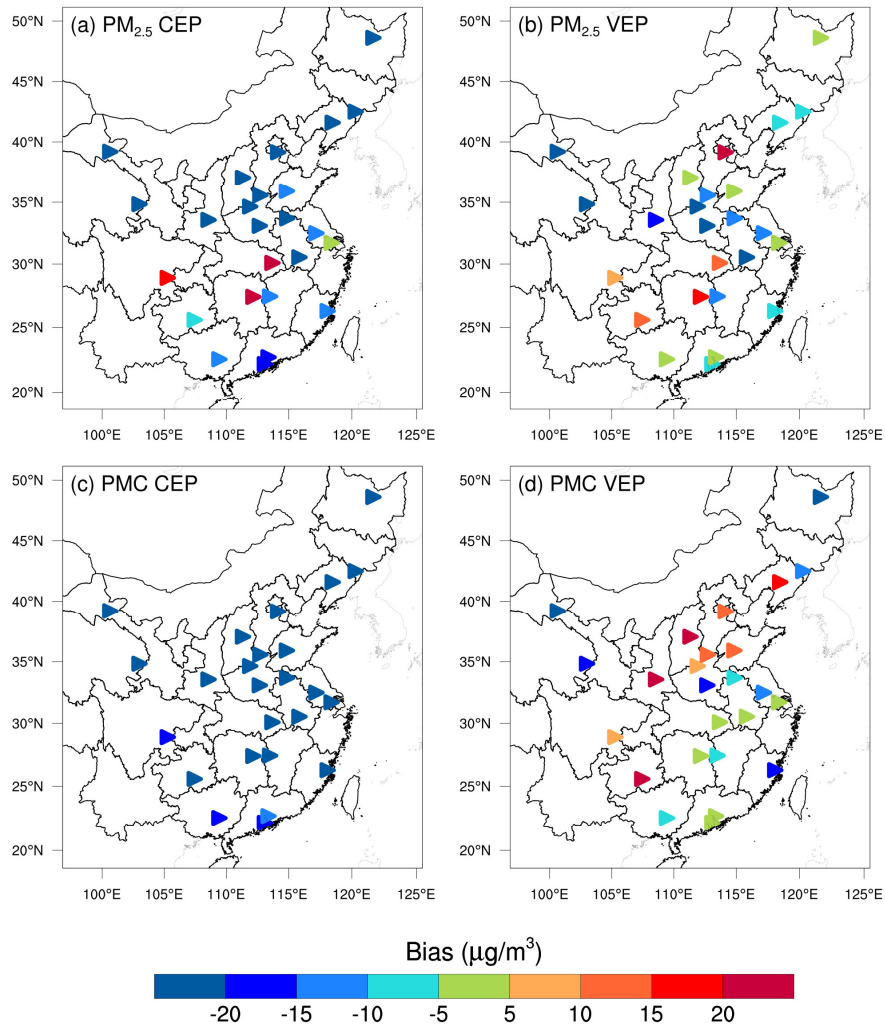
740 Figure 7 and Figure 8 show the spatial distributions of the biases calculated against the
 741 independent observations for the 5 species. With posterior emissions, the decreasing
 742 ratios of RMSEs range from 26.7% to 42.0%, and the CORRs increase by 13.7-59.0%
 743 to 0.62-0.87. Overall, the biases at the independent sites are similar or slightly worse
 744 than those at the assimilated sites, which is reasonable since the closer to the assimilated
 745 site the independent sites are, the more constraints of observation information can be
 746 obtained, and the improvements in optimized state variables of the model are more
 747 significant. For example, generally, the transmission distance of NO₂ is relatively short,
 748 and remote cities with small emission correlations to the cities with assimilated
 749 observations are relatively less constrained, resulting in only a 26.7% decrease in the
 750 RMSE.



751

752

Figure 7. As in Figure 5 but for the independent validation.



753
754 **Figure 8.** As in Figure 6 but for the independent validation.

755 Compared with the previous studies, Tang et al. (2013) conducted inversion of CO
 756 emissions over Beijing and the surrounding areas, the improvements (Table 6) in the
 757 RMSE (37-48% vs. 30-51%) and the CORR (both studies ~ 0.81) are comparable, but
 758 the biases here could decrease by 90-97%, which is much greater than their 48-64%
 759 reductions. Additionally, Chen et al. (2019) showed that the RMSE of simulated SO₂
 760 with updated SO₂ emissions decreased by 4.2-52.2% for different regions, and the
 761 CORR only increased to 0.69 at most. The improvement is relatively smaller than our
 762 results, which may be due to the insufficient adjustment of emissions caused by the
 763 underestimated ensemble spread through the inflation method. The better performance
 764 in this study may be related to our inversion process that makes the optimized emissions

765 of the current DA window propagate to the next DA window for further correction.

766 **Table 6.** Statistics comparing the pollution concentrations from the simulations with
 767 prior (CEP) and posterior (VEP) emissions against assimilated and independent
 768 observations, respectively. CO unit: mg m⁻³; others units: µg m⁻³.

Species	Mean Obs.	Mean Sim.		BIAS		RMSE		CORR	
		CEP	VEP	CEP	VEP	CEP	VEP	CEP	VEP
Against assimilated observations									
CO	1.43	0.66	1.36	-0.77	-0.08	1.08	0.56	0.46	0.81
SO ₂	32.5	34.4	28.4	1.9	-4.1	42.4	17.7	0.39	0.88
NO ₂	43.8	40.8	39.0	-2.9	-4.8	25.0	12.3	0.65	0.88
PM _{2.5}	77.0	53.1	70.3	-24.0	-6.7	50.3	29.6	0.64	0.87
PMC	40.5	8.1	37.5	-32.4	-3.1	41.5	24.6	0.25	0.69
Against independent observations									
CO	1.54	0.79	1.52	-0.75	-0.02	1.15	0.72	0.59	0.82
SO ₂	40.6	39.2	37.3	-1.3	-3.2	44.3	27.2	0.57	0.87
NO ₂	50.2	50.0	47.5	-0.3	-2.7	21.7	15.9	0.73	0.83
PM _{2.5}	91.5	64.6	84.1	-26.9	-7.4	64.1	37.2	0.62	0.87
PMC	42.0	9.2	40.4	-32.8	-1.6	39.3	26.6	0.39	0.62

769 * BIAS, mean bias; RMSE, root mean square error; CORR, correlation coefficient

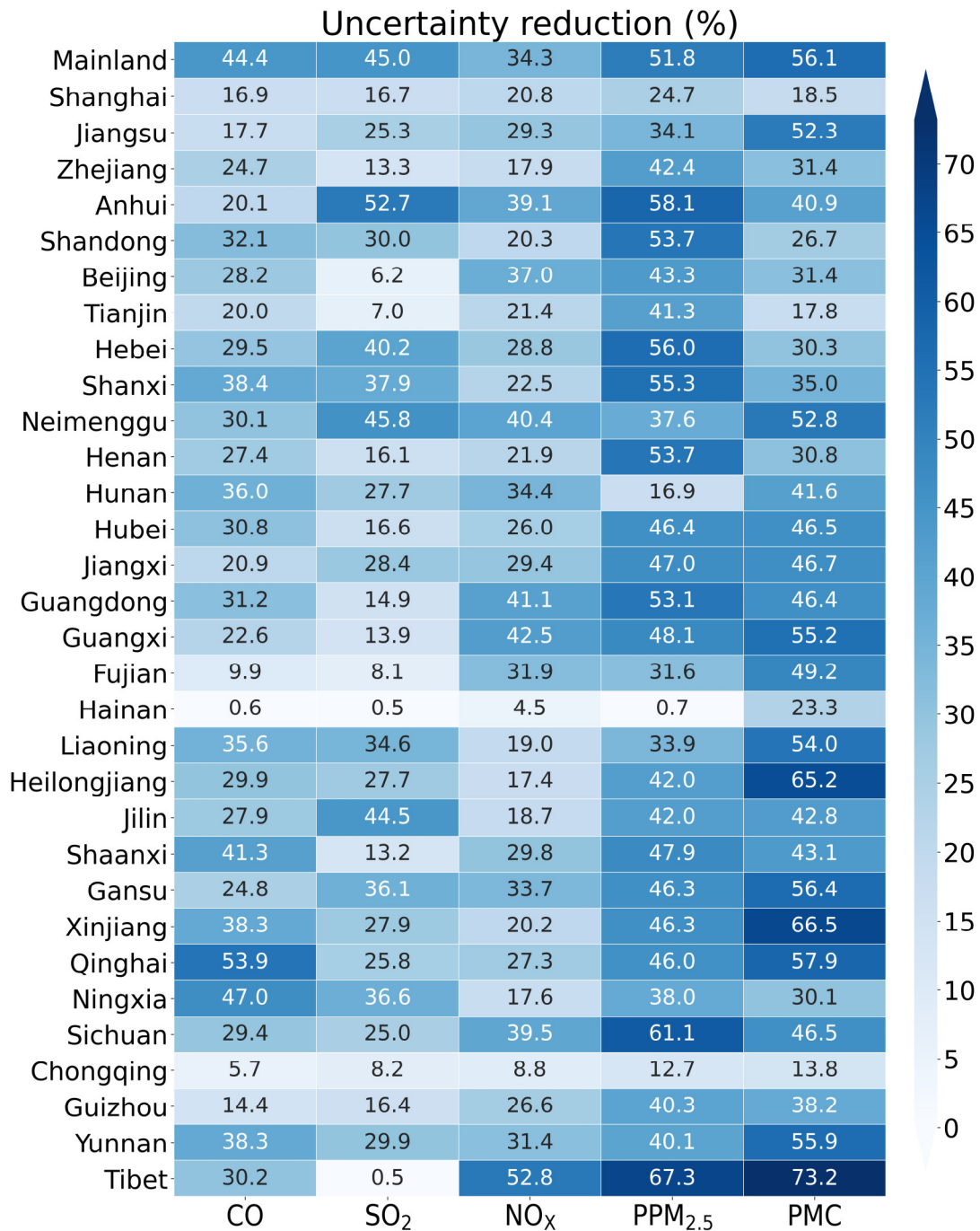
770 4.1.4 Uncertainty reduction

771 The uncertainty reduction rate (UR) is another important quantity to evaluate the
 772 performance of RAPAS and the effectiveness of in-situ observations in this system
 773 (Chevallier et al., 2007; Jiang et al., 2021; Takagi et al., 2011). Following Jiang et al.
 774 (2021), the UR is calculated as

$$775 \quad UR = \left(1 - \frac{\sigma_{posterior}}{\sigma_{prior}}\right) \times 100 \quad (19)$$

776 where $\sigma_{posterior}$ and σ_{prior} are the posterior and prior uncertainties, respectively,
 777 which were calculated using the standard deviations of the prior and posterior
 778 perturbations (Text S3). Figure 940 shows the URs averaged in each province and the
 779 whole mainland China. The URs vary with species, and among the 5 species of
 780 emissions, the uncertainties of the PPM_{2.5} and PMC are greatly reduced, while the UR
 781 of NO_x emission is lowest, that is because the URs are closely related to the magnitude

782 settings of prior uncertainties (Jiang et al., 2021). For the whole mainland China, the
783 uncertainties are reduced by 44.4%, 45.0%, 34.3%, 51.8% and 56.1% for CO, SO₂, NO_x,
784 PPM_{2.5} and PMC, respectively. For one species, it also varies across provinces. The
785 URs are usually related to observation coverage, which means that the more observation
786 constraints there are, the more the URs decrease. Additionally, the URs may also relate
787 to emission distributions. Generally, the URs are more significant in the provinces
788 where the observations and emissions are both relatively concentrated (e.g., Tibet),
789 while they are much lower in where the emissions are scattered or relatively uniform,
790 but the observations are only in large cities, even though there are many more
791 observations than other provinces. _



792

793 **Figure 910.** Time-averaged posterior emission uncertainty reduction (%) indicated by
 794 the standard deviation reduction of total emissions per province calculated by prior and
 795 posterior ensembles.

796 **4.1.5 Evaluation using chi-squared statistics**

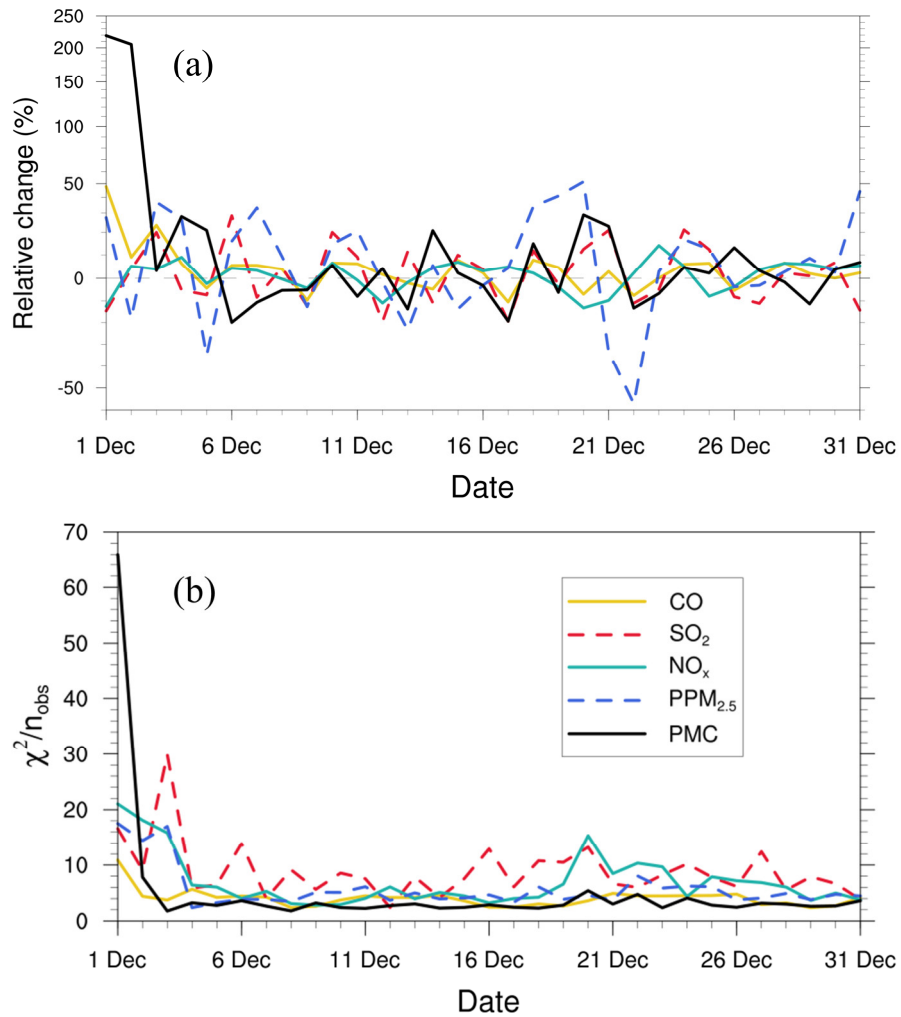
797 To diagnose the performance of the EnKF analysis, the chi-squared (χ^2) statistics was
 798 calculated, which is generally used to test whether the prior ensemble mean RMSE with

799 respect to the observations is consistent with the prior “total spread” (square root of the
800 sum of ensemble variance and observation error variance). Following Zhang et al.
801 (2015), for the t th window, χ^2 is defined as

$$\chi_t^2 = (\mathbf{y} - \mathbf{H}\bar{\mathbf{X}}^b)^T (\mathbf{H}\mathbf{P}^b\mathbf{H}^T + \mathbf{R})^{-1} (\mathbf{y} - \mathbf{H}\bar{\mathbf{X}}^b) \quad (20)$$

803 Figure 10 shows the time series of the relative changes between the prior and posterior
804 emissions and the χ^2 statistics. There are relatively large adjustments of emissions in
805 the first three windows, especially for PMC. After that, the optimality of the five species
806 reaches a more optimal state with successive emission inversion cycle. The χ^2 statistics
807 shows a similar variation characteristics with the daily changes in the emissions. The
808 χ^2 value is slightly greater than 1, indicating that the uncertainties from error covariance
809 statistics do not fully account for the error in the ensemble simulations. A similar
810 situation also appeared in Chen et al. (2019). Further investigations should be
811 conducted to generate larger spreads by accounting for the influence of model errors.
812 Since we imposed a same uncertainty of prior emission at each DA window to partially
813 compensate for the influence of model errors, χ^2 statistics showed small fluctuations,
814 indicating that the system updates emissions consistently and stably.

815

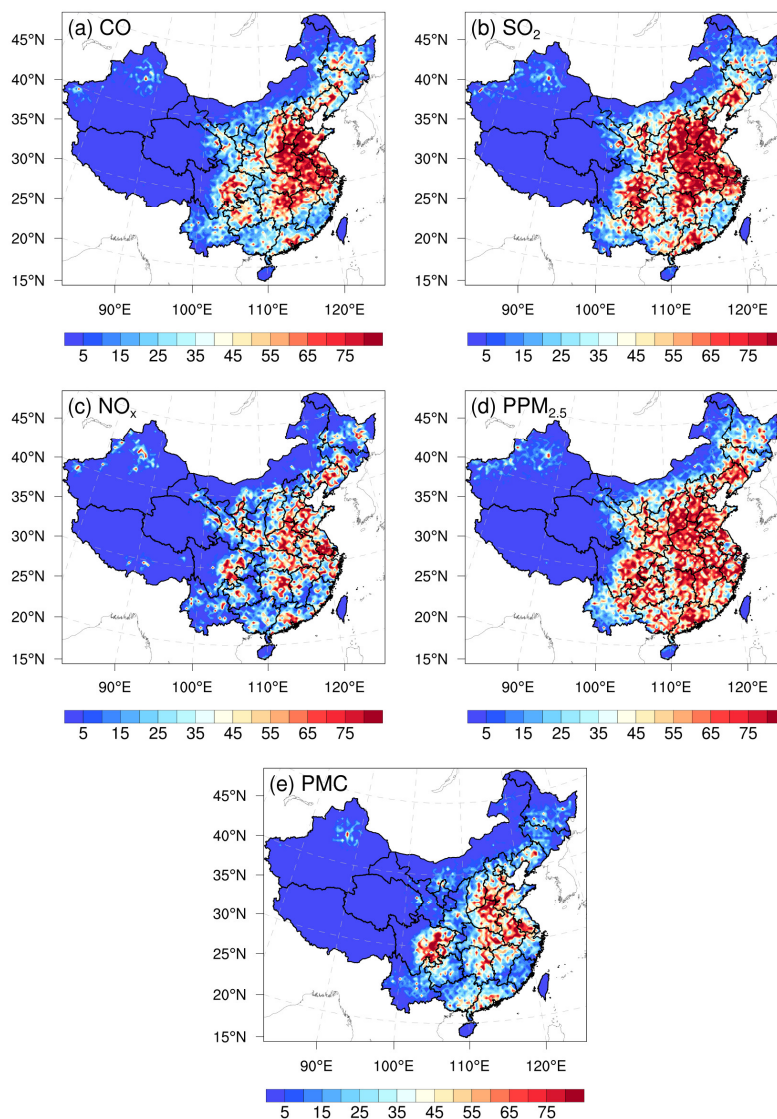


816

817 **Figure 10.** Relative changes (a) in a posteriori emission estimates of CO, SO₂, NO_x,
 818 PPM_{2.5} and PMC, and χ^2 statistics (b) of these state vectors in each window.

819 **4.1.6 Evaluation using OSSE**

820 Figure 11 shows the spatial distribution of the error reduction in the posterior emissions
 821 of the five species. It can be found that after inversion, in most areas, the emission errors
 822 can be reduced by more than 80%, especially in the central and eastern regions with
 823 dense observation sites, while in remote areas far away from cities, due to the sparse
 824 observation sites, the emission errors are still not well adjusted. Overall, the error
 825 reduction rates of CO, SO₂, NO_x, PPM_{2.5}, and PMC are 78.4%, 86.1%, 78.8%, 77.6%,
 826 and 72.0%, respectively, indicating that with the ground in-situ observations in China,
 827 RAPAS can significantly reduce emission errors, thus has good performance in



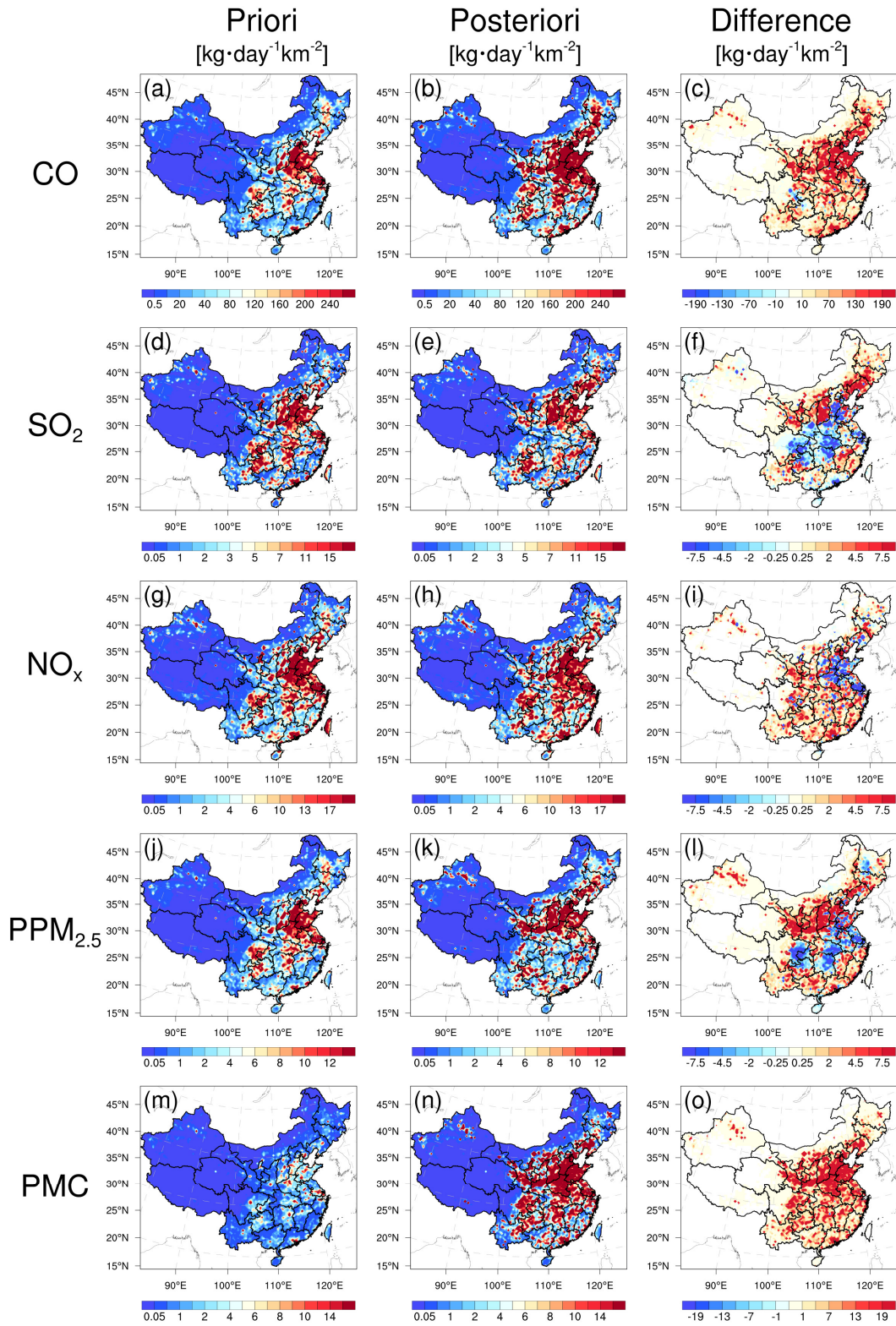
830 **Figure 11** Spatial distribution of the error reduction (%) of posterior emissions in the
 831 OSSE.

832 4.2 Inverted emissions

833 Figure 12+ shows the spatial distribution of the temporal averaged prior and posterior
 834 emissions and their differences of the emissions in December 2016.— It should be noted
 835 that the emissions outside China were masked, since the observation sites are all within
 836 China in this study, there is little change in the emissions outside China. Higher
 837 emissions are mainly concentrated in central and eastern China, especially in the NCP,

838 YRD, and PRD, and lower emissions occur across Northwest and Southern China.
839 Compared with the prior emissions, posterior CO emissions are considerably increased
840 across most areas of mainland China, especially in northern China, with an overall
841 increase of 129%. Notable underestimation of the prior emissions is also confirmed by
842 previous inversion estimations (Feng et al., 2020b; Tang et al., 2013; Wu et al., 2020)
843 and model evaluations (Kong et al., 2019~~ba~~). For SO₂, the emission increases mainly
844 occur in Northeast China, Shanxi, Ningxia, Gansu, Fujian, Jiangxi and Yunnan
845 provinces. In SCB, Central China, YRD, and part of NCP, the emissions are
846 significantly reduced. For national total, the SO₂ emission is increased by 20%. For
847 NO_x, although the increment of national total emissions is small, only about 5%, large
848 deviations still exist on regional scale. Obviously, the emissions in the NCP and YRD
849 are reduced, while in the other regions, the emissions of most cities are increased. The
850 changes in PPM_{2.5} emission are similar to SO₂. Compared with the prior emission, the
851 posterior PPM_{2.5} emissions are decreased over central China, SCB and YRD, while the
852 ones in southern and northern China are increased, especially in Shanxi, Shaanxi, Gansu
853 and southern Hebei province. Overall, the relative increase is 95%. For PMC, the
854 posterior emissions are increased over the whole mainland China, with national mean
855 relative increase exceeding 1000%. Larger emission increments mainly occur in the
856 areas where have significant anthropogenic emissions of CO and PPM_{2.5}, indicating
857 that the large underestimations of PMC emissions in the prior inventory may be mainly
858 attributed to the underestimations of anthropogenic activities. In addition, the absence
859 of natural dust is another reason, as the wind-blown dust scheme was not applied in this
860 study.~~In addition, without dust may be another reason, since no wind blowing dust~~
861 ~~scheme was applied in this study as mentioned above.~~ Overall, PM₁₀ emissions
862 (PPM_{2.5}+PMC) increased by 318%. If we assume that all the increment in PM₁₀
863 emissions is all from natural dust, that means the contribution of natural dust accounts
864 for 75% of total PM₁₀ emissions, which is consistent with the source apportionment of
865 PM₁₀ of 75% in Changsha in Central China (Li et al., 2010). Large PMC emission
866 increment are also found in Ma et al (2019).

867 Detailed estimation of posterior emissions and relative changes compared to prior
868 emissions in each province and the whole mainland China is given in Table S1. The
869 evaluation results for July show that the emission uncertainty can still be significantly
870 reduced, and the performance of the system in July is comparable to that in December
871 (Table S2). Additionally, the seasonal variation of emissions can be well reflected
872 (Figures S4 and S5), which means that our system can perform well at different times
873 of the year. Note that the differences, excluding PMC, between the prior and posterior
874 emissions mainly reflect the deficiencies of the prior emissions because the times of the
875 prior emissions and the observations are completely consistent in this study.



876

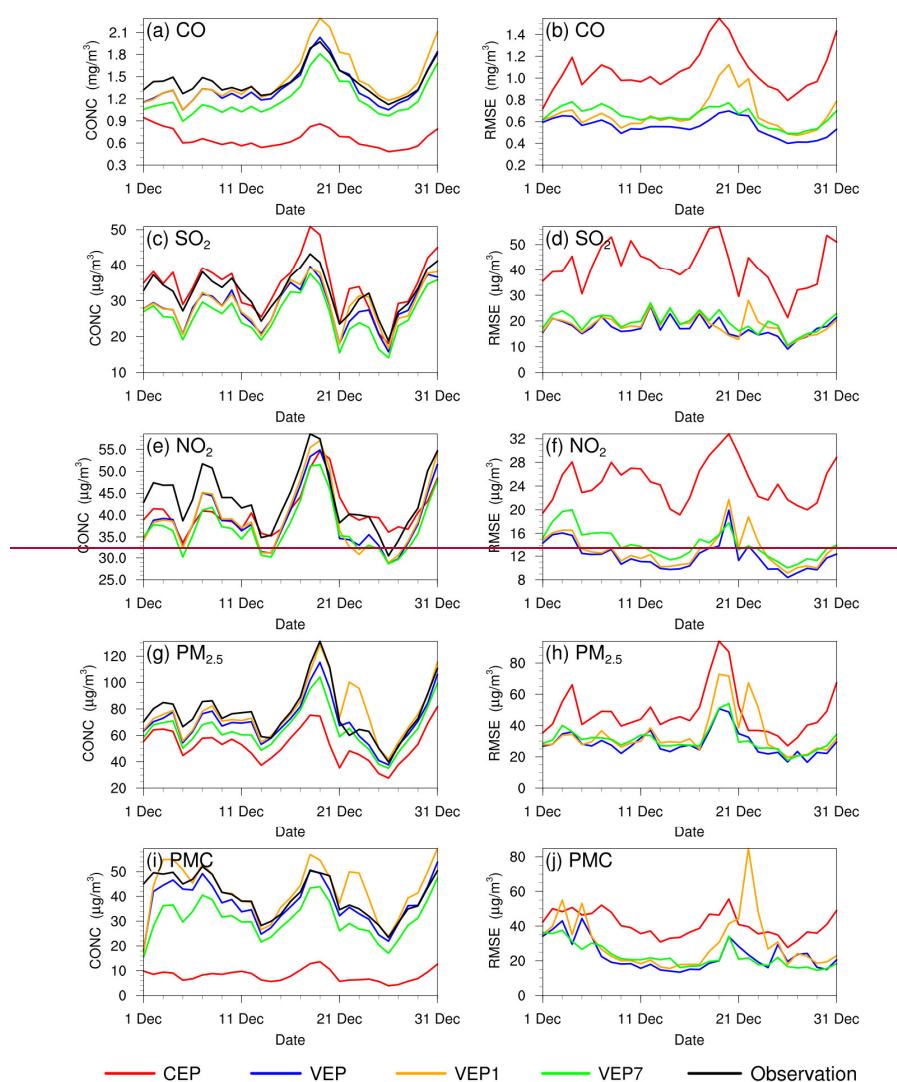
877 **Figure 12.4.** Spatial distribution of the time-averaged prior emissions (left column,
 878 MEIC 2016), posterior emissions (middle column), and differences (right column,
 879 posterior minus prior).

4.3 Sensitivity tests

4.3.1 The advantages of “two-step” scheme

Adjusting the ICs and emissions simultaneously (i.e., “one-step” scheme) has been applied to constrain prior emissions in many previous studies (Evensen, 2009; Kong et al., 2019b). To investigate the impact of different methods on the optimized emissions, a sensitivity test (EMS1) is performed, in which the initial fields of each DA window are optimized using the 3DVAR algorithm directly. Compared with our “two-step” method (EMDA), the posterior emissions of EMS1 are increased by 7%, 1.4%, 0.6%, 22.2%, and 17.2% for CO, SO₂, NO_x, PM_{2.5} and PMC, respectively. As mentioned previously, in the “two-step” scheme, the optimized emission can be sufficiently fed back to the concentration field and fully mixed in the atmosphere (1 day), and the error transfer makes the system consistently and stably updated. If the emission in one window is overestimated, in this way, it could be compensated in the next window with lower estimates. In contrast, when initial fields assimilating with observations simultaneously at each window, the overestimation will not be corrected and will accumulate to the end. We also evaluate the posterior emissions of EMS1 using the same method as shown in Sect. 4.1.3. Figure 13 shows the time series of simulated and observed daily concentrations and their RMSEs verified against the assimilated sites. Overall, compared to the base experiment (EMDA), the performance of EMS1 is significantly worse, with RMSEs of CO, SO₂, NO₂, PM_{2.5} and PMC increasing from 0.56 mg m⁻³, 17.7, 12.3, 29.6, and 24.6 μg m⁻³ to 0.69 mg m⁻³, 18.8, 13.3, 36.8, and 33.3 μg m⁻³, respectively. Additionally, it can be seen from the figure that the results of the two experiments are relatively close at the beginning and during the heavy pollution period (16-21 December). However, after that, the simulated results with “one-step” inversion emissions are significantly higher than the observations, and these large biases continue until the end. The results verified against the independent sites also show a similar situation (Figure S4). The reason may be that during the period of heavy pollution, the WRF-CMAQ (off-line model) does not consider the feedback process of meteorology and chemistry, resulting in low simulations. Therefore, the system will

909 ~~compensate for the underestimated concentrations caused by the model error through~~
 910 ~~more emissions, resulting in the overestimation of emissions. The accumulation of~~
 911 ~~emission error in each independent window further leads to the overestimation of~~
 912 ~~concentration after the end of high pollution, especially for species with a long lifetime~~
 913 ~~(e.g., CO). On the contrary, this overestimation will be corrected quickly in the~~
 914 ~~subsequent inversion using the “two-step” inversion scheme in this study, so as to~~
 915 ~~ensure the stability of the system. It should be noted that the model performance~~
 916 ~~depends on many factors but does not affect the advantage of the “two-step” scheme.~~



917 **Figure 13.** Time series of the daily concentrations (CONC, left) and root mean square
 918 error (RMSE, right) obtained from CEP, VEP, VEP1, and VEP3. The simulations were
 919 verified against the assimilated sites.
 920

921 **4.3.12 Impact of prior inventories**

922 Various prior inventories have great differences in space allocation and emission
923 magnitude. Inversion results can be sensitive to a priori emissions if the observation is
924 insufficient (Gurney et al., 2004; He et al., 2018). MEIC 2012 is used as an alternative
925 a priori in EMS2 to investigate the impact of different prior emissions on the posteriori.
926 Figure 134 shows the time series of the relative differences in daily posterior emissions
927 of the five species between the EMDA (base) and EMS2 experiments. Overall, the
928 differences between the two posterior emissions gradually decrease over time. At the
929 beginning, the differences in the CO, SO₂, NO_x, PPM_{2.5} and PMC between the two
930 inventories (i.e., MEIC 2012 vs MEIC 2016) are 17.5%, 114.5%, 30.8%, 46.0% and
931 72.0%, respectively, while during the last ten days, the differences of the two posterior
932 emissions have decreased to 2.5%, 4.5%, 4.5%, -8.9% and 3.0%, respectively. In
933 addition, it also could be found that the species that has larger emission differences at
934 the beginning take a longer time (namely more DA steps) to achieve convergence. The
935 quick convergence of PMC emission is attributed to the large prior uncertainty of 100%
936 used in the first 3 DA windows. Different from the other species, there are significant
937 negative deviations of PPM_{2.5} emissions between the two experiments. That may be
938 due to the positive deviations in the precursors of PM_{2.5} (i.e., SO₂ and NO_x), which will
939 lead to a larger amount of secondary production. To balance the total PM_{2.5}
940 concentration, the PPM_{2.5} emissions will be reduced. We compare the PM_{2.5}
941 concentrations simulated by the two optimized inventories and find that they are almost
942 the same (Figure S65). Overall, this indicates that the observation in China is sufficient
943 in inferring the emissions, and our system is rather robust. Meanwhile, it also suggests
944 that the monthly posterior emissions shown in Sect. 4.2 are still underestimated to a
945 certain extent.

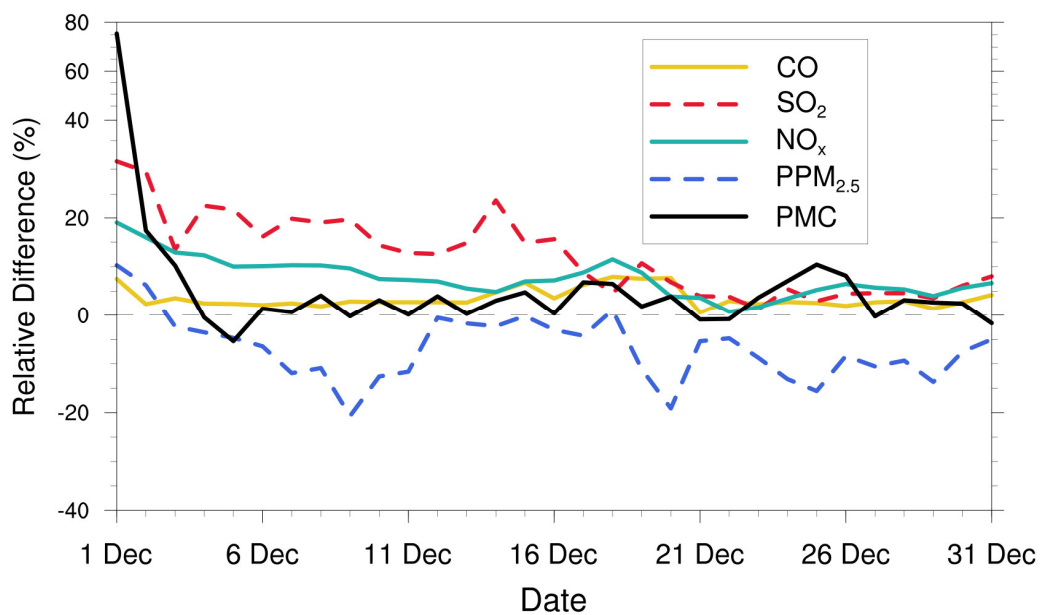


Figure 134. Relative differences in CO, SO₂, NO_x, PPM_{2.5} and PMC emissions (% the ratio of absolute difference to EMDA) between the EMDA and EMS2 experiments.

4.3.23 Impact of prior uncertainties settings

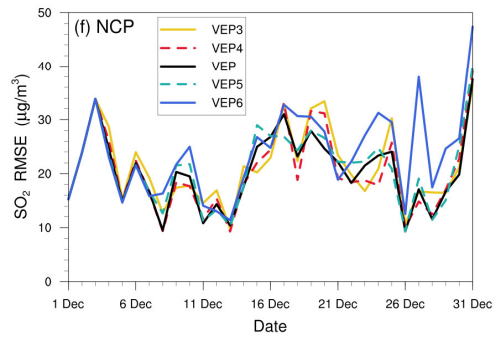
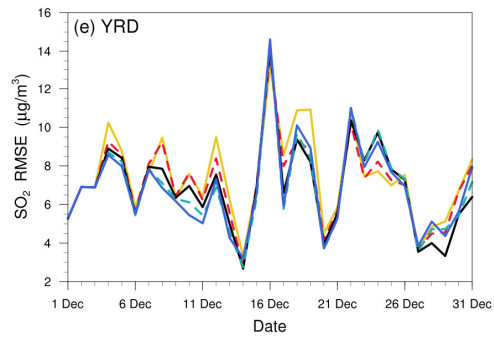
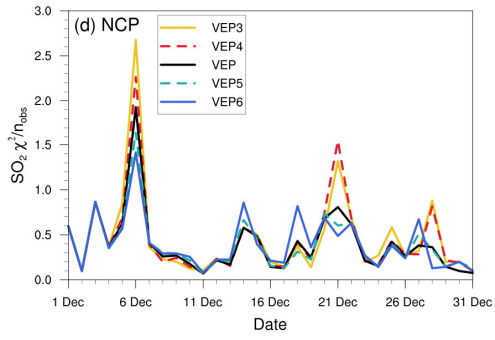
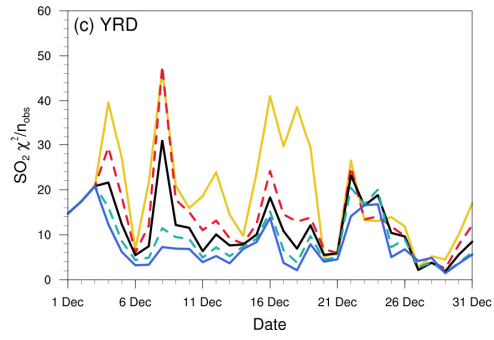
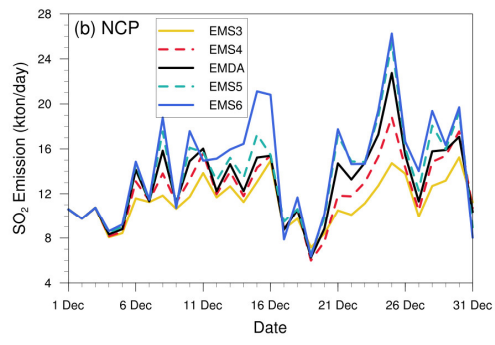
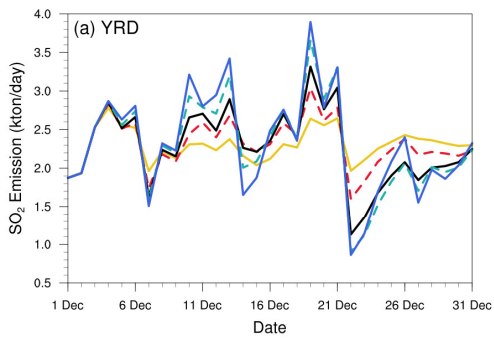
The uncertainty of prior emissions determines how closely the analysis is weighted toward the background and observation, but information about prior uncertainties is generally not readily available. To evaluate the possible influence of prior uncertainties on the optimized emissions, we increased/reduced the uncertainties after 3 days of cycling, namely starting at 0000 UTC, 3 December, by 25% and 50 % in EMS3 (-50%), EMS4 (-25%), EMS5 (+25%) and EMS6 (+50%), respectively. Table 7 summarizes the emission changes with different prior uncertainties settings in EMS3-6 experiments. To better understand the response of the system to the emission uncertainty settings, Figure 145 shows the time series of SO₂ emission changes, [the Chi-square statistics](#) and the RMSEs of simulated SO₂ with emissions updated in the EMDA and EMS3-6 experiments over the YRD and NCP (Figure 2). Compared with the EMDA, when the uncertainties are decreased (increased), the emissions of the 5 species decrease (increase) accordingly. That is because the posterior emissions of the 5 species are larger than the prior emissions, and as shown in [Figure 14a-d](#)~~Fig-13~~, larger uncertainty

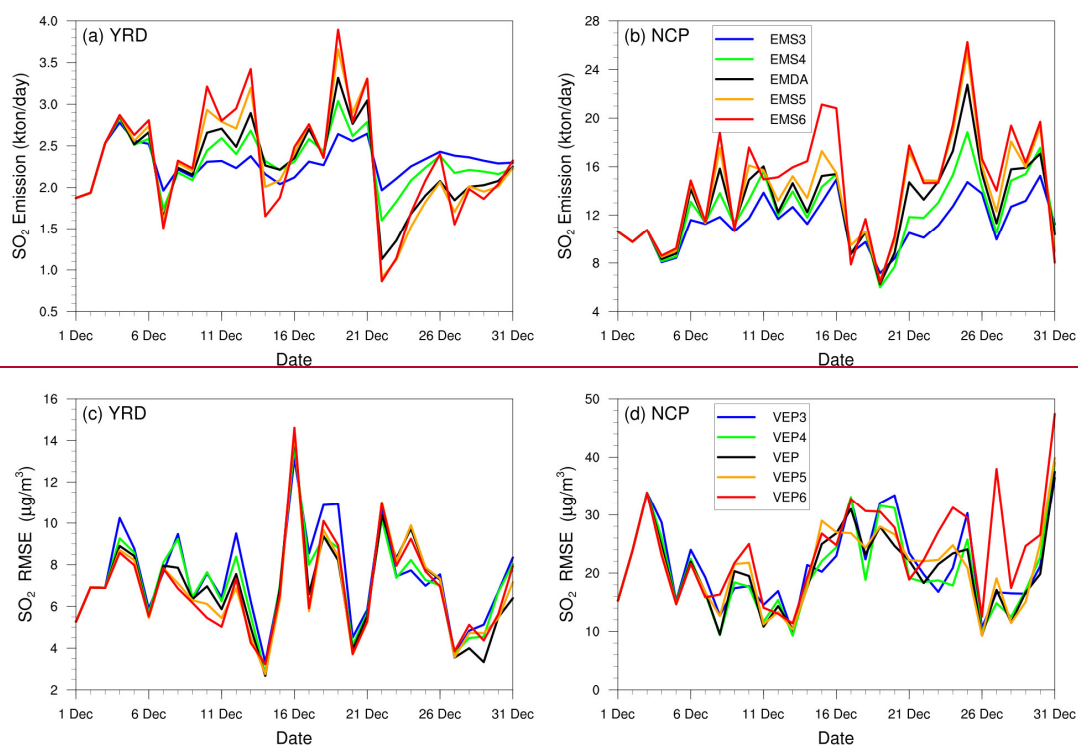
965 will lead to a faster convergence, resulting in larger posterior emissions. It also could
 966 be found from Figure 145 that a faster convergence will indeed reduce the RMSE of
 967 the simulated concentration with the posterior emissions in the early stage of the
 968 experiment, but in the later stage of the experiment, there are no significant differences
 969 for the RMSE and Chi-square statistics among the different experiments. However, the
 970 day-to-day changes in emissions can also cause slight fluctuations. In addition, it shows
 971 that when greater uncertainties are set, the day-to-day changes in emissions are also
 972 more drastic, resulting in a larger RMSE as shown in NCP. Moreover, those significant
 973 day-to-day variations of estimated emissions may not be in line with the actual situation.
 974 Due to the spatial-temporal inhomogeneity of emissions, the differences of Chi-square
 975 statistics between the YRD and NCP show that it may be necessary to apply different a
 976 priori uncertainties according to different regions (Chen et al., 2019). Therefore, when
 977 using an EnKF system for emission estimation, we have to be very careful about the
 978 setting of these errors. Overall, the uncertainties chosen in EMDA aim to minimize the
 979 deviation of the concentration fields and maintain the stability of inversion.

980 **Table 7.** Relative differences in CO, SO₂, NO_x, PPM_{2.5} and PMC emissions (% , the
 981 ratio of absolute difference to EMDA) between the EMDA and EMS3-6 experiments.

Species	EMS3	EMS4	EMS5	EMS6
CO	-8.6	-4	3	5.2
SO ₂	-14	-5.7	3.6	6.8
NO _x	-6.5	-3	2.8	4.5
PPM _{2.5}	-16.5	-7.8	4.6	8.7
PMC	-18.5	-8.2	7.3	13.1

982





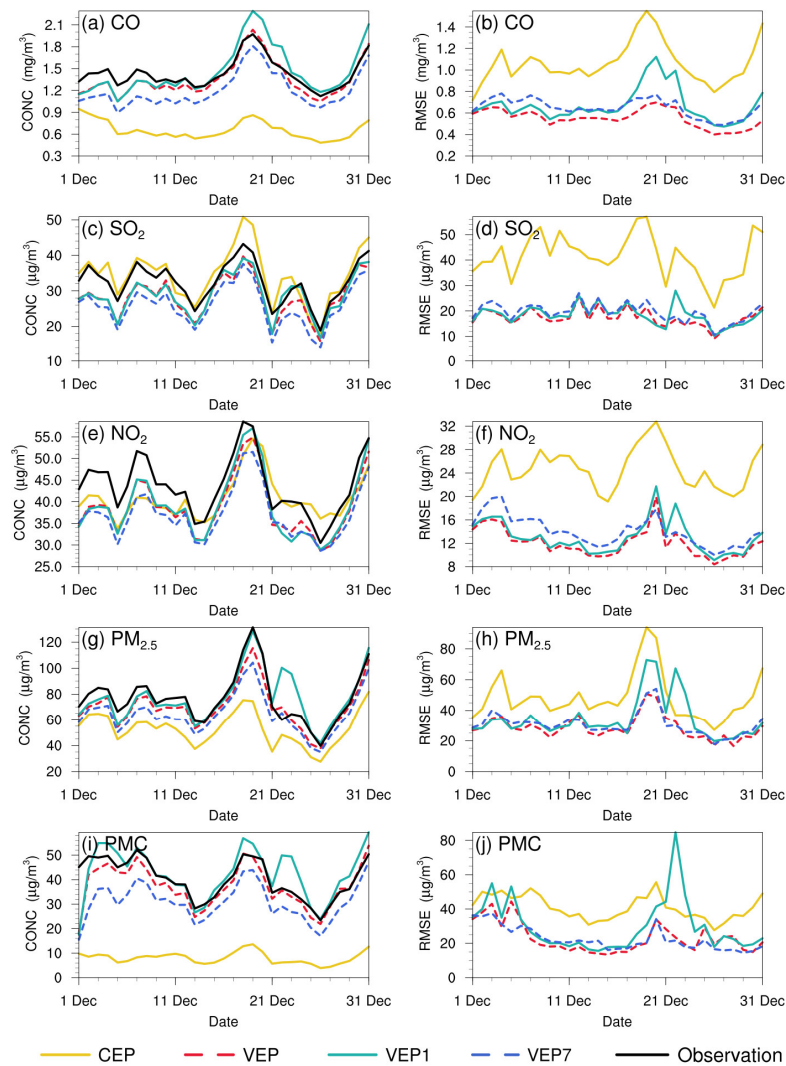
984

985 **Figure 145.** Time-series of SO₂ emission changes, the Chi-square statistic
 986 emissions
 987 changes and the RMSE of simulated SO₂ with updated SO₂ emissions in the EMDA
 988 and EMS3-6 experiments over the Yangtze River Delta (YRD) and North China Plain (NCP).

989 **4.3.34 Impact of observation error settings**

990 Another factor that determines the relative weights of the observation and background
 991 in the analysis is observation errors. A proper estimate of the observation error is also
 992 important in regard to the filter performance, but observation errors are not provided
 993 with the dataset. The observation error is usually set to a fixed value (Ma et al., 2019),
 994 a specific proportion of the observation value (Tang et al., 2013) or the value calculated
 995 by combining measurement error with representative error as used in this study.
 996 Generally, the performance of the data assimilation is quite sensitive to the specification
 997 of observation error (Tang et al., 2013). To evaluate the influence of observation error
 998 on the optimized emissions, a sensitivity experiment (EMS7) with doubled observation
 999 error was conducted. Overall, the spatial distribution of emissions after optimization is

1000 almost the same as that of the EMDA experiment, but the increment is lower (Figure
 1001 S76), resulting in a weaker estimate of the national total emission for each species. That
 1002 is because that the observation error becomes large, the system will be more convinced
 1003 of the prior emission and reduce the effect of observation information. Figure 15 shows
 1004 the time series of simulated and observed daily concentrations and their RMSEs
 1005 verified against the assimilated sites. The simulations in VEP7 usually perform worse,
 1006 with larger biases and RMSEs than those of VEP (Figures 13, S84 and S97), especially
 1007 in most of western and southern China where posterior emissions are still significantly
 1008 underestimated. These results usually correspond to sluggish emission changes and
 1009 large Chi-square statistics (Figure S10), suggesting that too large observation error may
 1010 substantially impact the estimated emissions.



1011

1012 **Figure 15.** Time series of the daily concentrations (CONC, left) and root mean square
1013 error (RMSE, right) obtained from CEP, VEP, VEP1, and VEP7. The simulations were
1014 verified against the assimilated sites.

1015 **4.3.4 Impact of the IC optimization of the first window**

1016 Many studies have shown that there would be large emission discrepancies resulting
1017 from the IC errors (Jiang et al., 2013a; Miyazaki et al., 2017; Tang et al., 2013), which
1018 means that if the IC is not optimized, the errors of concentrations would be compensated
1019 through the adjustment of emissions. To evaluate the impact of the IC optimization of
1020 the first window on the emission inversions, the EMS8 experiment without the IA step
1021 was conducted. Figure 16 shows the time series of the relative differences in daily
1022 posterior emissions of the five species between the EMDA and EMS8 experiments. It
1023 can be found that the optimization of IC has great impact on the emission inversions of
1024 long-lived species (i.e., CO). The overall difference in the inverted CO emissions
1025 between the two experiments is about 5.3%, and in the first few windows, the maximum
1026 difference can reach 26.1%. For the short-lived species, the IC optimization has little
1027 impact on the emission, for example, the averaged emission differences of SO₂, NO_x
1028 and PMC in the two experiments are 0.3%, 0.3% and 0.9%, respectively. For PPM2.5,
1029 it is affected not only by the primary emission, but also by the complex chemistry of its
1030 precursors. Therefore, the difference between the two experiments fluctuates at a
1031 certain extent, with overall difference of 2%. It is worth noting that with the gradual
1032 disappearance of the benefit of IC assimilation, the two experiments can reach a unified
1033 state after some windows. For CO, the impact of IA on emission inversion lasts about
1034 half a month. These results indicate that removing the bias of IC of the first DA window
1035 is essential for subsequent inverse analysis (Jiang et al., 2017).

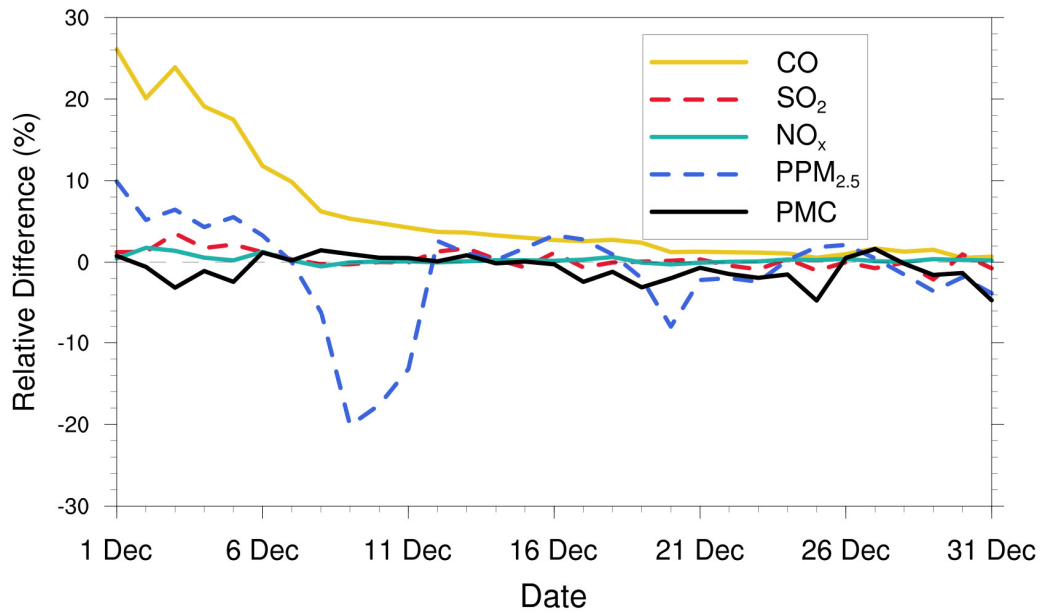


Figure 16. Relative differences in CO, SO₂, NO_x, PPM_{2.5} and PMC emissions (% , the ratio of absolute difference to EMDA) between the EMDA and EMS8.

4.3.5 The advantages of “two-step” scheme

Adjusting the ICs and emissions simultaneously (i.e., “one-step” scheme) has been applied to constrain prior emissions in many previous studies (Evensen, 2009; Kong et al., 2019a). To investigate the impact of different methods on the optimized emissions, a sensitivity test (EMS1) was performed, in which the initial fields of each DA window were optimized using the 3DVAR algorithm directly. Compared with our “two-step” method (EMDA), the posterior emissions of EMS1 are increased by 7%, 1.4%, 0.6%, 22.2%, and 17.2% for CO, SO₂, NO_x, PM_{2.5} and PMC, respectively. Overall, there is no significant difference between the two methods for NO_x and SO₂, but for CO, it can be clearly seen that the difference increases with the inversion (Figure S11). As mentioned previously, in the “two-step” scheme, the unresolved posterior emission error will be fed back to the initial field of the next window through sufficient mixed simulation within one day for timely optimization. Meanwhile, the system always maintains the mass balance of pollutants. In this way, the system updates emissions more consistently and stably. If the emission in one window is overestimated, in this way, it could be

1054 compensated in the next window with lower estimates. In contrast, when initial fields
1055 assimilating with observations simultaneously at each window, the overestimation will
1056 not be corrected and will accumulate to the end. We also evaluate the posterior
1057 emissions of EMS1 using the same method as shown in Sect. 4.1.3. Overall, compared
1058 to the base experiment (EMDA), the performance of EMS1 is significantly worse, with
1059 RMSEs of CO, SO₂, NO₂, PM_{2.5} and PMC increasing from 0.56 mg m⁻³, 17.7, 12.3,
1060 29.6, and 24.6 μg m⁻³ to 0.69 mg m⁻³, 18.8, 13.3, 36.8, and 33.3 μg m⁻³, respectively
1061 (Figure 15). Additionally, it can be seen from the figure that the results of the two
1062 experiments are relatively close at the beginning and during the heavy pollution period
1063 (16-21 December). However, after that, the simulated results with “one-step” inversion
1064 emissions are significantly higher than the observations, and these large biases continue
1065 until the end. The results verified against the independent sites also show a similar
1066 situation (Figure S8). The reason may be that during the period of heavy pollution, the
1067 WRF-CMAQ (off-line model) does not consider the feedback process of meteorology
1068 and chemistry, resulting in low simulations. Therefore, the system will compensate for
1069 the underestimated concentrations caused by the model error through more emissions,
1070 resulting in the overestimation of emissions. The accumulation of emission error in each
1071 independent window further leads to the overestimation of concentration after the end
1072 of high pollution, especially for species with a long lifetime (e.g., CO). On the contrary,
1073 this overestimation will be corrected quickly in the subsequent inversion using the
1074 “two-step” inversion scheme in this study (Figure S11), so as to ensure the stability of
1075 the system. Additionally, the other “one-step” experiment, taking MEIC 2012 as prior
1076 emissions, was conducted. However, the relative differences (Figure S12) in posterior
1077 emissions between this experiment and the EMS1 did not converge like that between
1078 EMDA and EMS2 with “two-step” scheme (Figure 13), which further demonstrates the
1079 advantages of the “two-step” scheme. It should be noted that the model performance
1080 depends on many factors but does not affect the advantage of the “two-step” scheme.

1081 **4.4 Discussion**

1082 Optimal state estimation using an EnKF relies on the assumption of unbiased Gaussian

1083 prior error, which is not guaranteed in such highly nonlinear and large biases systems
1084 In this study, some pollutants (e.g., CO, PMC) have very large simulated biases, thus if
1085 a small uncertainty is adopted, the emission bias cannot be fully reduced, while if a
1086 very large uncertainty is adopted, then the degree of freedom of adjustment is too large,
1087 and the inverted daily emissions will fluctuate abnormally. Therefore, we only set a
1088 larger prior uncertainty in the first three windows, adopted a moderate uncertainty in
1089 the following windows, and used a “two-step” inversion scheme and cyclic iteration to
1090 gradually correct the emission errors. Figure 10(a) shows the time series of the relative
1091 differences between the prior and posterior emissions in each window. There are the
1092 relatively large adjustments for the emissions in the first three windows, especially for
1093 PMC, but the adjustment ranges of the five species after the first 3 windows are
1094 basically within the uncertainty range (e.g., $\pm 25\%$), indicating that with this scheme,
1095 the EnKF method used in this system still has a good performance in emission inversion.
1096 The model-data mismatch error not only comes from the emissions, but also from the
1097 inherent model errors arising from model structure, discretization, parameterizations
1098 and the biases in the simulated meteorological fields. Neglecting model errors would
1099 attribute all uncertainties to emissions, and lead to considerable biases in the estimated
1100 emissions. In the version of CMAQ model used in this study, there is no heterogeneous
1101 reactions (Quan et al., 2015; Wang et al., 2017), the parameterization scheme for the
1102 formation of secondary organic aerosol (SOA) is imperfect (Carlton et al., 2008; Jiang
1103 et al., 2012; Yang et al., 2019), no feedback between chemistry and meteorology is
1104 considered, and we used an idea profile for chemical lateral boundary conditions. All
1105 of the above problems can lead to underestimated concentrations of pollutants, which
1106 in turn require more emissions to compensate, leading to overestimations in emissions.
1107 In addition, previous studies have shown that the emission of ammonia in the MEIC
1108 inventory was underestimated (Kong et al., 2019b; Paulot et al., 2014; Zhang et al.,
1109 2018). Due to lack of ammonia observations, our system does not include emission
1110 estimates of ammonia, which means that the concentration of ammonium aerosol was
1111 underestimated in this system, also resulting in an overestimation in the $PPM_{2.5}$

1112 emission. Wind-blown dust was also not simulated here, thus the PMC emission
1113 inverted in this system do not only come from anthropogenic activities, but also from
1114 natural sources. Although some of these shortcomings could be solved in the future by
1115 updating the CTM model, there will still be errors in each parameterization and each
1116 process. Generally, parameter estimation method was used to reduce the model errors,
1117 in which, some uncertain parameters were included in the augmented state vector and
1118 were optimized synchronously based on the available observations (Brandhorst et al.,
1119 2017; Evensen, 2009). However, it is still quite difficult to identify the key uncertain
1120 parameters of different species in different models, which generally comes not only
1121 from the complex atmospheric chemical model, but also from hundreds of model inputs
1122 (Tang et al., 2013). Another method is bias correction, which treats the model error as
1123 a bias term, and includes it in the augmented state vector (Brandhorst et al., 2017; De
1124 Lannoy et al., 2007; Keppenne et al., 2005). In addition, the weak-constraint 4D-Var
1125 method can also be used to reduce the model errors, which adds a correction term in
1126 the model integration to account for the different sources of model error (Sasaki, 1970).
1127 Although reliable diagnosis of model error is still a challenge at present (Laloyaux et
1128 al., 2020), it should be considered in an assimilation system. We will consider model
1129 errors in our system in the future to obtain better emission estimates.

1130 Independent variable localization was adopted to avoid potential spurious correlations
1131 across different species in this study. However, the transmission scales for different
1132 species in different regions are still different, and a more accurate localization range
1133 could be obtained through backward trajectory analysis. Although Hamer et al. (2015)
1134 successfully used O₃ observations to estimate NO_x and VOC emissions within the 4D-
1135 var framework within an idealised model. In additionally, O₃ observations are not
1136 assimilated to improve NO_x and VOC emissions using cross-species information due to
1137 the strong nonlinear effects within the O₃-NO_x-VOC relationship (Wang et al., 2019b),
1138 in which the O₃ concentration and NO_x (VOC) emissions are positively correlated in
1139 the NO_x (VOC)-limited region and negatively correlated in the VOC (NO_x)-limited
1140 region (Tang et al., 2011). This work will be followed up by an ongoing work using

1141 available VOC observations. The optimization of the initial fields or emissions of NO₂
1142 may also change the O₃-NO_x-VOC relationship. Assuming that NO₂ is underestimated,
1143 the NO₂ concentration increases after assimilation, but the VOC concentration remains
1144 unchanged, then in the NO_x (VOC)-limited region, the subsequent generation of O₃
1145 will increase (decrease); Conversely, the ozone concentration errors caused by
1146 assimilating NO₂ will also affect the subsequent NO_x emission inversion. Similarly, the
1147 model may not be able to resolve local-scale NO₂ well because of uniform distribution
1148 of concentration over the whole grid. Therefore, the model is shifted towards a NO_x
1149 (VOC)-limited regime in high (low) pollution regions, which negatively impacts results
1150 by perturbing ozone chemistry in unrealistic ways (Inness et al., 2015). To evaluate the
1151 influence of O₃-NO_x-VOC relationship change and model resolution on inversion, we
1152 also further conducted a nested emission inversion on a densely observed area (the
1153 Yangtze River Delta, China) with a grid spacing of 12 km (Feng et al., 2022). The study
1154 period is the same as this study. Results showed that the NO_x emissions in the Yangtze
1155 River Delta retrieved at two resolutions are almost the same (14.7 kt/day vs. 13.4
1156 kt/day), with a difference of 8.8%, indicating that the emissions can be adjusted
1157 effectively by RAPAS. As shown previously, the concentrations after DA are obviously
1158 underestimated in western China, indicating that the inverted emissions over these
1159 regions still have large uncertainties because of the sparsity of observations that are
1160 spatially insufficient for sampling the inhomogeneity of emissions. Therefore, further
1161 investigations with joint assimilation of multisource observations (e.g., satellite) are
1162 also underway.

1163 When comparing the performances of the “two-step” and “one-step” schemes, for the
1164 “one-step” scheme, we use a combination assimilation method, namely 3DVAR for the
1165 optimizations of initial fields and EnKF for emission inversions in each DA window,
1166 which is similar as Jiang et al., (2017), but different from most previous studies
1167 (Miyazaki et al., 2017; Tang et al., 2013). Because most previous “one-step”
1168 assimilation studies used only one method (i.e., EnKF). This combination method may
1169 cause the comparison less than perfect. However, it should be noted that, even using

1170 the same method (such as EnKF) to optimize the emission of the current window and
1171 the initial field of the next window simultaneously (Peng et al., 2018), the initial field
1172 estimation errors will still be mixed in the simulated concentration field, resulting in
1173 unreasonable emission compensation in the next window. In “one-step” scheme, the
1174 essence is to build a good initial field in the high levels. Schwartz et al. (2014) compared
1175 the performances of EnKF and 3DVAR in optimizing initial fields, and found that
1176 3DVAR method can obtain a better initial field than EnKF method. Therefore, we
1177 believe that in this comparison, a combinatorial assimilation approach used in the "one-
1178 step" scheme is an acceptable approach, and the conclusion is credible, that the “two-
1179 step” scheme has better performances than the “one-step” scheme in emission estimates.
1180 NO_x is mainly emitted by transportation (Li et al., 2017), which can better reflect the
1181 level of economic activities to a certain extent. Weekly emission changes were also
1182 explored to verify the performance of the system in depicting emission changes (Figure
1183 S13). Although the “weekend effect” of emissions in China is not significant (Wang et
1184 al., 2014; Wang et al., 2015), the posterior NO_x emission changes showed a good
1185 agreement with the observations. In our previous studies (Feng et al., 2020a; Feng et
1186 al., 2020b), the system was successfully applied to optimize NO_x and CO emissions,
1187 respectively. The inverted emission changes were also in line with the time points of
1188 epidemic control. Additionally, the emission changes can well reflect the emission
1189 migration from developed regions or urban areas to developing regions or surrounding
1190 areas over recent years, which were consistent with the emission control strategies in
1191 China. Although the system does not consider the model error, resulting in a certain
1192 difference between the posterior emission and the actual emission, the spatiotemporal
1193 changes in posterior emissions are relatively reasonable, which can be used to monitor
1194 emission changes and make emission regulations.

1196 **5 Summary and conclusions**

1197 In this study, we developed a Regional multi-Air Pollutant Assimilation System

1198 (RAPASv1.0) based on the WRF/CMAQ model, 3DVAR and EnKF algorithm. RAPAS
1199 can quantitatively optimize gridded emissions of CO, SO₂, NO_x, PPM_{2.5} and PMC on
1200 regional scale by simultaneously assimilating hourly in-situ measurements of CO, SO₂,
1201 NO₂, PM_{2.5} and PM₁₀. This system includes two subsystems, namely the IA subsystem
1202 and the EI subsystem, which optimizes the chemical ICs, and infers the anthropogenic
1203 emissions, respectively.

1204 Taking the 2016 Multi-resolution Emission Inventory for China (MEIC 2016) in
1205 December as a priori, the emissions of CO, SO₂, NO_x, PPM_{2.5} and PMC in December
1206 2016 were inferred through assimilating the corresponding nationwide observations
1207 over China. The optimized ICs and posterior emissions were examined against the
1208 assimilated and independent observations through parallel forward simulation
1209 experiments with and without DA. Sensitivity tests are also performed to investigate
1210 the impact of different inversion processes, prior emissions, prior uncertainties and
1211 observation errors on the emission estimates.

1212 The results show that RAPAS has a good performance in assimilating ground in-situ
1213 observations, with the calculated emission uncertainties can significantly improve the
1214 simulations and reduce the uncertainties of the emissions. For the whole mainland
1215 China, the emission uncertainties reduced by 44.4%, 45.0%, 34.3%, 51.8% and 56.1%
1216 for CO, SO₂, NO_x, PPM_{2.5} and PMC, respectively. It can also significantly improve the
1217 simulations, the RMSEs of the simulated concentrations with posterior emissions
1218 decreased by 40.1-56.3%, and the CORRs increased from 0.26-0.66 to 0.69-0.87 for
1219 different species. The OSSE experiment shows that the error of posterior CO, SO₂, NO_x,
1220 PPM_{2.5}, and PMC could be reduced by 78.4%, 86.1%, 78.8%, 77.6%, and 72.0%,
1221 respectively. Overall, compared with the prior emissions (MEIC 2016), the posterior
1222 emissions increased by 129%, 20%, 5% and 95% for CO, SO₂, NO_x and PPM_{2.5},
1223 respectively. The posterior PMC emissions, which included anthropogenic and natural
1224 dust contributions, increased by 1045%. The sensitivity tests with different inversion
1225 processes show that the “two-step” scheme in emission inversion outperforms the joint
1226 adjustment of ICs and emissions (“one-step” scheme), especially after heavy pollution.

1227 The sensitivity tests with different prior inventories show the observation in China is
1228 sufficient in inferring the emissions, and our system is less dependent on prior
1229 inventories. Additionally, the sensitivity tests with different prior uncertainties indicate
1230 that when the posterior emissions are larger than the prior emissions, the emissions
1231 decrease/increase with the decreases/increases of uncertainties because of the different
1232 convergence rates. These results demonstrate the advantage of the two-step method in
1233 emission inversion in that the inversion errors of the last window could be transferred
1234 to the current window for further optimization and the robustness of the emissions
1235 estimated from RAPAS using the nationwide observations over China. It should be
1236 noted that the system usually responds slowly to too small a priori uncertainty or too
1237 large observation error, which may result in large errors in the estimated emissions.⁹
1238 and S10_

1239
~~1240 Independent variable localization was adopted to avoid potential spurious correlations
1241 across different species in this study. However, the transmission scales for different
1242 species in different regions are still different, and a more accurate localization range
1243 could be obtained through backward trajectory analysis. In additionally, O₃
1244 observations are not assimilated to improve NO_x and VOC emissions using cross-
1245 species information due to the strong nonlinear effects within the O₃-NO_x-VOC
1246 relationship, in which the O₃ concentration and NO_x (VOC) emissions are positively
1247 correlated in the NO_x (VOC) limited region and negatively correlated in the VOC
1248 (NO_x) limited region (Tang et al., 2011). This work will be followed up by an ongoing
1249 work using available VOC observations. As shown previously, the concentrations after
1250 DA are obviously underestimated in western China, indicating that the inverted
1251 emissions over these regions still have large uncertainties because of the sparsity of
1252 observations that are spatially insufficient for sampling the inhomogeneity of emissions.
1253 Therefore, further investigations with joint assimilation of multisource observations
1254 (e.g., satellite) are also underway.~~

1255 In summary, the comprehensive evaluation and sensitivity tests reveal that RAPAS
1256 could serve as this study offers a useful tool for accurately quantifying the spatial and
1257 temporal changes of multi-species emissions at regional scales and near-real time,
1258 which will be helpful for the air pollution control in China, and the other regions around
1259 the world with dense ground observation networks~~multi-species anthropogenic~~
1260 ~~emissions at large scales and near-real time, which will serve better for monitoring~~
1261 ~~emission changes and designing future emissions regulations and pollution control.~~

1263 **Code and data availability**

1264 The codes of RAPAS v1.0 are available at <https://doi.org/10.5281/zenodo.5566225>.

1265 ~~The codes of RAPAS v1.0 are available at <https://doi.org/10.5281/zenodo.5566225>.~~

1266 The WRF model code is open-source code and can be obtained from the WRF Model
1267 User's Page (<https://www2.mmm.ucar.edu/wrf/users>, last access: 25 April 2021). The
1268 CMAQ model is available through an open license as well (<https://www.epa.gov/cmaq> ,
1269 last access: 25 April 2021). The observation and emission data used in this paper are
1270 available at <https://doi.org/10.5281/zenodo.4718290> (Feng and Jiang, 2021).

1272 **Author contribution**

1273 SF, FJ, ZW and ZJ developed RAPAS v1.0. SF and FJ designed the research. SF
1274 performed model simulations, analyzed data, and prepared the paper with contributions
1275 from all co-authors. FJ supervised the model development project and assisted in
1276 conceptualization and writing. HW, WH, YS, LZ, YZ, CL, and WJ contributed to the
1277 discussion and improvement of the paper.

1279 **Competing interests**

1280 The authors declare that they have no conflict of interest.

1281 **Acknowledgements**

1282 This work is supported by the National Key R&D Program of China (Grant No.
1283 2016YFA0600204), the National Natural Science Foundation of China (Grant No.
1284 41907378), and the Nanjing University Innovation and Creative Program for Ph.D.
1285 candidate (Grant No. CXCY19-60). We are grateful to the High Performance
1286 Computing Center (HPCC) of Nanjing University for doing the numerical calculations
1287 in this paper on its blade cluster system, and thank the MEIC team for providing the
1288 prior anthropogenic emissions (<http://www.meicmodel.org/>).

1290 **References**

1291 Appel, K. W., Pouliot, G. A., Simon, H., Sarwar, G., Pye, H. O. T., Napelenok, S. L., Akhtar, F., and
1292 Roselle, S. J.: Evaluation of dust and trace metal estimates from the Community Multiscale Air
1293 Quality (CMAQ) model version 5.0, *Geoscientific Model Development*, 6, 883-899,
1294 10.5194/gmd-6-883-2013, 2013.

1295 [Alexe, M., Bergamaschi, P., Segers, A., Detmers, R., Butz, A., Hasekamp, O., Guerlet, S., Parker,](#)
1296 [R., Boesch, H., Frankenberg, C., Scheepmaker, R. A., Dlugokencky, E., Sweeney, C., Wofsy, S.](#)
1297 [C., and Kort, E. A.: Inverse modelling of CH₄ emissions for 2010-2011 using different satellite](#)
1298 [retrieval products from GOSAT and SCIAMACHY, *Atmospheric Chemistry and Physics*, 15,](#)
1299 [113-133, 2015.](#)

1300 Barbu, A. L., Segers, A. J., Schaap, M., Heemink, A. W., and Bultjes, P. J. H.: A multi-component
1301 data assimilation experiment directed to sulphur dioxide and sulphate over Europe,
1302 *Atmospheric Environment*, 43, 1622-1631, 2009.

1303 [Basu, S., Guerlet, S., Butz, A., Houweling, S., Hasekamp, O., Aben, I., Krummel, P., Steele, P.,](#)
1304 [Langenfelds, R., Torn, M., Biraud, S., Stephens, B., Andrews, A., and Worthy, D.: Global CO₂](#)
1305 [fluxes estimated from GOSAT retrievals of total column CO₂, *Atmospheric Chemistry and*](#)
1306 [*Physics*, 13, 8695-8717, 2013.](#)

1307 Bauwens, M., Compernelle, S., Stavrou, T., Müller, J.-F., van Gent, J., Eskes, H., Levelt, P. F.,
1308 van der A, R., Veeffkind, J. P., Vlietinck, J., Yu, H., and Zehner, C.: Impact of Coronavirus
1309 Outbreak on NO₂ Pollution Assessed Using TROPOMI and OMI Observations, 47,
1310 e2020GL087978, 10.1029/2020gl087978, 2020.

1311 [Bierman: Factorization methods for Discrete Sequential estimation, Academic Press, 1977.](#)

1312 Binkowski, F. S. and Roselle, S. J.: Models-3 community multiscale air quality (CMAQ) model
1313 aerosol component - 1. Model description, *Journal of Geophysical Research-Atmospheres*, 108,
1314 10.1029/2001jd001409, 2003.

1315 [Brandhorst, N., Erdal, D., and Neuweiler, I.: Soil moisture prediction with the ensemble Kalman](#)
1316 [filter: Handling uncertainty of soil hydraulic parameters, *Advances in Water Resources*, 110, 360-](#)
1317 [370, 2017.](#)

1318 Bruhwiler, L. M. P., Michalak, A. M., Peters, W., Baker, D. F., and Tans, P.: An improved Kalman
1319 Smoother for atmospheric inversions, *Atmos. Chem. Phys.*, 5, 2691-2702, 10.5194/acp-5-2691-
1320 2005, 2005.

1321 [Carlton, A. G., Turpin, B. J., Altieri, K. E., Seitzinger, S. P., Mathur, R., Roselle, S. J., and Weber,
1322 R. J.: CMAQ Model Performance Enhanced When In-Cloud Secondary Organic Aerosol is
1323 Included: Comparisons of Organic Carbon Predictions with Measurements, *Environmental
1324 Science & Technology*, 42, 8798-8802, 2008](#)

1325 Chen, D., Liu, Z., Ban, J., and Chen, M.: The 2015 and 2016 wintertime air pollution in China: SO₂
1326 emission changes derived from a WRF-Chem/EnKF coupled data assimilation system,
1327 *Atmospheric Chemistry and Physics*, 19, 8619-8650, 10.5194/acp-19-8619-2019, 2019.

1328 Chen, D., Liu, Z., Fast, J., and Ban, J.: Simulations of sulfate-nitrate-ammonium (SNA) aerosols
1329 during the extreme haze events over northern China in October 2014, *Atmospheric Chemistry
1330 and Physics*, 16, 10707-10724, 10.5194/acp-16-10707-2016, 2016.

1331 Chevallier, F., Bréon, F.-M., and Rayner, P. J.: Contribution of the Orbiting Carbon Observatory to
1332 the estimation of CO₂ sources and sinks: Theoretical study in a variational data assimilation
1333 framework, 112, 10.1029/2006JD007375, 2007.

1334 Clements, A. L., Fraser, M. P., Upadhyay, N., Herckes, P., Sundblom, M., Lantz, J., and Solomon,
1335 P. A.: Chemical characterization of coarse particulate matter in the Desert Southwest - Pinal
1336 County Arizona, USA, *Atmospheric Pollution Research*, 5, 52-61, 10.5094/apr.2014.007, 2014.

1337 Clements, N., Hannigan, M. P., Miller, S. L., Peel, J. L., and Milford, J. B.: Comparisons of urban
1338 and rural PM_{10-2.5} and PM_{2.5} mass concentrations and semi-volatile fractions in northeastern
1339 Colorado, *Atmospheric Chemistry and Physics*, 16, 7469-7484, 10.5194/acp-16-7469-2016, 2016.

1340 [Daley, R.: Atmospheric Data Assimilation \(gtSpecial Issue>Data Assimilation in Meteorology and
1341 Oceanography: Theory and Practice\), *Journal of the Meteorological Society of Japan. Ser. II*, 75,
1342 319-329, 1997.](#)

1343 [Derber, J. C.: A VARIATIONAL CONTINUOUS ASSIMILATION TECHNIQUE, *Monthly
1344 Weather Review*, 117, 2437-2446, 1989.](#)

1345 de Foy, B., Lu, Z., Streets, D. G., Lamsal, L. N., and Duncan, B. N.: Estimates of power plant NO_x
1346 emissions and lifetimes from OMI NO₂ satellite retrievals, *Atmospheric Environment*, 116, 1-11,
1347 10.1016/j.atmosenv.2015.05.056, 2015.

1348 [De Lannoy, G. J. M., Houser, P. R., Pauwels, V. R. N., and Verhoest, N. E. C.: State and bias
1349 estimation for soil moisture profiles by an ensemble Kalman filter: Effect of assimilation depth
1350 and frequency, 43, 2007.](#)

1351 Ding, J., van der A, R. J., Mijling, B., Levelt, P. F., and Hao, N.: NO_x emission estimates during the
1352 2014 Youth Olympic Games in Nanjing, *Atmospheric Chemistry and Physics*, 15, 9399-9412,
1353 10.5194/acp-15-9399-2015, 2015.

1354 Elbern, H., Strunk, A., Schmidt, H., and Talagrand, O.: Emission rate and chemical state estimation
1355 by 4-dimensional variational inversion, *Atmospheric Chemistry and Physics*, 7, 3749-3769,
1356 10.5194/acp-7-3749-2007, 2007.

1357 Evensen, G.: The Ensemble Kalman Filter for Combined State and Parameter Estimation MONTE
1358 CARLO TECHNIQUES FOR DATA ASSIMILATION IN LARGE SYSTEMS, *Ieee Control
1359 Systems Magazine*, 29, 83-104, 10.1109/mcs.2009.932223, 2009.

1360 Feng, S., Jiang, F., Jiang, Z., Wang, H., Cai, Z., and Zhang, L.: Impact of 3DVAR assimilation of
1361 surface PM_{2.5} observations on PM_{2.5} forecasts over China during wintertime, *Atmospheric*
1362 *Environment*, 187, 34-49, 10.1016/j.atmosenv.2018.05.049, 2018.

1363 [Feng, S., Jiang, F., Wang, H., Shen, Y., Zheng, Y., Zhang, L., Lou, C., and Ju, W.: Anthropogenic](#)
1364 [emissions estimated using surface observations and their impacts on PM_{2.5} source apportionment](#)
1365 [over the Yangtze River Delta, China, *Science of The Total Environment*, 828, 154522, 2022](#)

1366 Feng, S., Jiang, F., Wu, Z., Wang, H., Ju, W., and Wang, H.: CO Emissions Inferred From Surface
1367 CO Observations Over China in December 2013 and 2017, *Journal of Geophysical Research-*
1368 *Atmospheres*, 125, 10.1029/2019jd031808, 2020a.

1369 Feng, S., Jiang, F., Wang, H., Wang, H., Ju, W., Shen, Y., Zheng, Y., Wu, Z., and Ding, A.: NO_x
1370 Emission Changes Over China During the COVID-19 Epidemic Inferred From Surface NO₂
1371 Observations, *Geophysical Research Letters*, 47, 10.1029/2020gl090080, 2020b.

1372 Feng, S. and Jiang, F.: Anthropogenic air pollutant emissions over China inferred by Regional multi-
1373 Air Pollutant Assimilation System (RAPAS v1.0), Zenodo, 10.5281/zenodo.4718290, 2021.

1374 Gaspari, G. and Cohn, S. E.: Construction of correlation functions in two and three dimensions,
1375 *Quarterly Journal of the Royal Meteorological Society*, 125, 723-757, 10.1256/smsqj.55416, 1999.

1376 Guenther, A. B., Jiang, X., Heald, C. L., Sakulyanontvittaya, T., Duhl, T., Emmons, L. K., and Wang,
1377 X.: The Model of Emissions of Gases and Aerosols from Nature version 2.1 (MEGAN2.1): an
1378 extended and updated framework for modeling biogenic emissions, *Geoscientific Model*
1379 *Development*, 5, 1471-1492, 10.5194/gmd-5-1471-2012, 2012.

1380 Gurney, K. R., Law, R. M., Denning, A. S., Rayner, P. J., Pak, B. C., Baker, D., Bousquet, P.,
1381 Bruhwiler, L., Chen, Y. H., Ciais, P., Fung, I. Y., Heimann, M., John, J., Maki, T., Maksyutov, S.,
1382 Peylin, P., Prather, M., and Taguchi, S.: Transcom 3 inversion intercomparison: Model mean
1383 results for the estimation of seasonal carbon sources and sinks, *Global Biogeochemical Cycles*,
1384 18, 10.1029/2003gb002111, 2004.

1385 He, W., van der Velde, I. R., Andrews, A. E., Sweeney, C., Miller, J., Tans, P., van der Laan-Luijkx,
1386 I. T., Nehrkorn, T., Mountain, M., Ju, W., Peters, W., and Chen, H.: CTDAS-Lagrange v1.0: a
1387 high-resolution data assimilation system for regional carbon dioxide observations, *Geoscientific*
1388 *Model Development*, 11, 3515-3536, 10.5194/gmd-11-3515-2018, 2018.

1389 Hinds, W.C.: *Aerosol Technology: Properties, Behavior, and Measurement of Airborne Particles*.
1390 New York: John Wiley, 1982.

1391 Houtekamer, P. L. and Mitchell, H. L.: A sequential ensemble Kalman filter for atmospheric data
1392 assimilation, *Monthly Weather Review*, 129, 123-137, 10.1175/1520-
1393 0493(2001)129<0123:asekff>2.0.co;2, 2001.

1394 Houtekamer, P. L. and Zhang, F.: Review of the Ensemble Kalman Filter for Atmospheric Data
1395 Assimilation, *Monthly Weather Review*, 144, 4489-4532, 10.1175/mwr-d-15-0440.1, 2016.

1396 [Inness, A., Blechschmidt, A. M., Bouarar, I., Chabrilat, S., Crepulja, M., Engelen, R. J., Eskes, H.,](#)
1397 [Flemming, J., Gaudel, A., Hendrick, F., Huijnen, V., Jones, L., Kapsomenakis, J., Katragkou, E.,](#)
1398 [Keppens, A., Langerock, B., de Maziere, M., Melas, D., Parrington, M., Peuch, V. H., Razinger,](#)
1399 [M., Richter, A., Schultz, M. G., Suttie, M., Thouret, V., Vrekoussis, M., Wagner, A., and Zerefos,](#)
1400 [C.: Data assimilation of satellite-retrieved ozone, carbon monoxide and nitrogen dioxide with](#)
1401 [ECMWF's Composition-IFS, *Atmospheric Chemistry and Physics*, 15, 5275-5303, 2015.](#)

1402 Jiang, F., Liu, Q., Huang, X., Wang, T., Zhuang, B., and Xie, M.: Regional modeling of secondary
1403 organic aerosol over China using WRF/Chem, *Journal of Aerosol Science*, 43, 57-73,
1404 10.1016/j.jaerosci.2011.09.003, 2012a.

1405 Jiang, F., Zhou, P., Liu, Q., Wang, T., Zhuang, B., and Wang, X.: Modeling tropospheric ozone
1406 formation over East China in springtime, *Journal of Atmospheric Chemistry*, 69, 303-319,
1407 10.1007/s10874-012-9244-3, 2012b.

1408 Jiang, F., Wang, H. M., Chen, J. M., Machida, T., Zhou, L. X., Ju, W. M., Matsueda, H., and Sawa,
1409 Y.: Carbon balance of China constrained by CONTRAIL aircraft CO₂ measurements,
1410 *Atmospheric Chemistry and Physics*, 14, 10133-10144, 10.5194/acp-14-10133-2014, 2014.

1411 Jiang, F., Wang, H., Chen, J. M., Ju, W., Tian, X., Feng, S., Li, G., Chen, Z., Zhang, S., Lu, X., Liu,
1412 J., Wang, H., Wang, J., He, W., and Wu, M.: Regional CO₂ fluxes from 2010 to 2015 inferred
1413 from GOSAT XCO₂ retrievals using a new version of the Global Carbon Assimilation System,
1414 *Atmos. Chem. Phys.*, 21, 1963-1985, 10.5194/acp-21-1963-2021, 2021.

1415 Jiang, W., Smyth, S., Giroux, E., Roth, H., and Yin, D.: Differences between CMAQ fine mode
1416 particle and PM_{2.5} concentrations and their impact on model performance evaluation in the lower
1417 Fraser valley, *Atmospheric Environment*, 40, 4973-4985, 10.1016/j.atmosenv.2005.10.069, 2006.

1418 Jiang, Z., Jones, D. B. A., Worden, H. M., Deeter, M. N., Henze, D. K., Worden, J.,
1419 Bowman, K. W., Brenninkmeijer, C. A. M., and Schuck, T. J.: Impact of model
1420 errors in convective transport on CO source estimates inferred from MOPITT CO
1421 retrievals, *Journal Of Geophysical Research-Atmospheres*, 118, 2073-2083, 2013a.

1422 Jiang, Z., Liu, Z., Wang, T., Schwartz, C. S., Lin, H.-C., and Jiang, F.: Probing into the impact of
1423 3DVAR assimilation of surface PM₁₀ observations over China using process analysis, *Journal of*
1424 *Geophysical Research: Atmospheres*, 118, 6738-6749, 10.1002/jgrd.50495, 2013b.

1425 Jiang, Z., Worden, J. R., Worden, H., Deeter, M., Jones, D. B. A., Arellano, A. F., and Henze, D. K.:
1426 A 15-year record of CO emissions constrained by MOPITT CO observations, *Atmospheric*
1427 *Chemistry And Physics*, 17, 4565-4583, 10.5194/acp-17-4565-2017, 2017.

1428 Jin, J., Lin, H. X., Heemink, A., and Segers, A.: Spatially varying parameter estimation for dust
1429 emissions using reduced-tangent-linearization 4DVar, *Atmospheric Environment*, 187, 358-373,
1430 10.1016/j.atmosenv.2018.05.060, 2018.

1431 Kahnert, M.: Variational data analysis of aerosol species in a regional CTM: background error
1432 covariance constraint and aerosol optical observation operators, *Tellus B*, 60, 2008.

1433 Kang, J.-S., Kalnay, E., Miyoshi, T., Liu, J., and Fung, I.: Estimation of surface carbon fluxes with
1434 an advanced data assimilation methodology, 117, 10.1029/2012JD018259, 2012.

1435 Keppenne, C. L., Rienecker, M. M., Kurkowski, N. P., and Adamec, D. A.: Ensemble Kalman filter
1436 assimilation of temperature and altimeter data with bias correction and application to seasonal
1437 prediction, *Nonlin. Processes Geophys.*, 12, 491-503, 2005.

1438 Kleist, D. T., Parrish, D. F., Derber, J. C., Treadon, R., Wu, W.-S., and Lord, S.: Introduction of the
1439 GSI into the NCEP Global Data Assimilation System, *Weather and Forecasting*, 24, 1691-1705,
1440 10.1175/2009waf2222201.1, 2009.

1441 Kong, L., Tang, X., Zhu, J., Wang, Z., Pan, Y., Wu, H., Wu, L., Wu, Q., He, Y., Tian, S., Xie, Y., Liu,
1442 Z., Sui, W., Han, L., and Carmichael, G.: Improved Inversion of Monthly Ammonia Emissions in
1443 China Based on the Chinese Ammonia Monitoring Network and Ensemble Kalman Filter,

1444 Environmental Science & Technology, 53, 12529-12538, 10.1021/acsest.9b02701, 2019a.

1445 Kong, L., Tang, X., Zhu, J., Wang, Z., Fu, J. S., Wang, X., Itahashi, S., Yamaji, K., Nagashima, T.,
1446 Lee, H. J., Kim, C. H., Lin, C. Y., Chen, L., Zhang, M., Tao, Z., Li, J., Kajino, M., Liao, H., Sudo,
1447 K., Wang, Y., Pan, Y., Tang, G., Li, M., Wu, Q., Ge, B., and Carmichael, G. R.: Evaluation and
1448 uncertainty investigation of the NO₂, CO and NH₃ modeling over China under the framework of
1449 MICS-Asia III, Atmos. Chem. Phys. Discuss., 2019, 1-33, 10.5194/acp-2018-1158, 2019b.

1450 Kurokawa, J.-i., Yumimoto, K., Uno, I., and Ohara, T.: Adjoint inverse modeling of NO_x emissions
1451 over eastern China using satellite observations of NO₂ vertical column densities, Atmospheric
1452 Environment, 43, 1878-1887, 10.1016/j.atmosenv.2008.12.030, 2009.

1453 [Laloyaux, P., Bonavita, M., Chrust, M., and Gürol, S.: Exploring the potential and limitations of](#)
1454 [weak-constraint 4D-Var, Quarterly Journal of the Royal Meteorological Society, 146, 4067-4082,](#)
1455 [2020](#)

1456 [Li, J.-d., Deng, Q.-h., Lu, C., and Huang, B.-l.: Chemical compositions and source apportionment](#)
1457 [of atmospheric PM₁₀ in suburban area of Changsha, China. Journal of Central South University](#)
1458 [of Technology, 17, 509-515, 2010.](#)

1459 Li, M., Zhang, Q., Kurokawa, J.-i., Woo, J.-H., He, K., Lu, Z., Ohara, T., Song, Y., Streets, D. G.,
1460 Carmichael, G. R., Cheng, Y., Hong, C., Huo, H., Jiang, X., Kang, S., Liu, F., Su, H., and Zheng,
1461 B.: MIX: a mosaic Asian anthropogenic emission inventory under the international collaboration
1462 framework of the MICS-Asia and HTAP, Atmospheric Chemistry and Physics, 17, 935-963,
1463 10.5194/acp-17-935-2017, 2017.

1464 Liu, Z., Liu, Q., Lin, H.-C., Schwartz, C. S., Lee, Y.-H., and Wang, T.: Three-dimensional variational
1465 assimilation of MODIS aerosol optical depth: Implementation and application to a dust storm
1466 over East Asia, Journal of Geophysical Research: Atmospheres, 116, n/a-n/a,
1467 10.1029/2011jd016159, 2011.

1468 [Lorenc, A. C.: Modelling of error covariances by 4D-Var data assimilation, Quarterly Journal of the](#)
1469 [Royal Meteorological Society, 129, 3167-3182, 2003.](#)

1470 [Hamer, P. D., Bowman, K. W., Henze, D. K., Attie, J. L., and Marecal, V.: The impact of observing](#)
1471 [characteristics on the ability to predict ozone under varying polluted photochemical regimes,](#)
1472 [Atmospheric Chemistry and Physics, 15, 10645-10667, 2015.](#)

1473 Ma, C., Wang, T., Mizzi, A. P., Anderson, J. L., Zhuang, B., Xie, M., and Wu, R.: Multiconstituent
1474 Data Assimilation With WRF-Chem/DART: Potential for Adjusting Anthropogenic Emissions
1475 and Improving Air Quality Forecasts Over Eastern China, 124, 7393-7412,
1476 10.1029/2019jd030421, 2019.

1477 Meirink, J. F., Eskes, H. J., and Goede, A. P. H.: Sensitivity analysis of methane emissions derived
1478 from SCIAMACHY observations through inverse modelling, Atmospheric Chemistry and
1479 Physics, 6, 1275-1292, 10.5194/acp-6-1275-2006, 2006.

1480 [Maybeck: Stochastic Models, Estimation and Control Academic Press, 1979.](#)

1481 Miyazaki, K. and Eskes, H.: Constraints on surface NO_x emissions by assimilating satellite
1482 observations of multiple species, Geophysical Research Letters, 40, 4745-4750,
1483 10.1002/grl.50894, 2013.

1484 Miyazaki, K., Eskes, H. J., and Sudo, K.: Global NO_x emission estimates derived from an
1485 assimilation of OMI tropospheric NO₂ columns, Atmospheric Chemistry and Physics, 12, 2263-

1486 2288, 10.5194/acp-12-2263-2012, 2012a.

1487 Miyazaki, K., Eskes, H. J., Sudo, K., Takigawa, M., van Weele, M., and Boersma, K. F.:
1488 Simultaneous assimilation of satellite NO₂, O₃, CO, and HNO₃ data for the analysis of
1489 tropospheric chemical composition and emissions, *Atmospheric Chemistry and Physics*, 12,
1490 9545-9579, 10.5194/acp-12-9545-2012, 2012b.

1491 [Miyazaki, K., Eskes, H., Sudo, K., Boersma, K. F., Bowman, K., and Kanaya, Y.:
1492 Decadal changes in global surface NO_x emissions from multi-constituent satellite
1493 data assimilation, *Atmospheric Chemistry and Physics*, 17, 807-837, 2017.](#)

1494 [Monteil, G., Houweling, S., Butz, A., Guerlet, S., Schepers, D., Hasekamp, O.,
1495 Frankenberg, C., Scheepmaker, R., Aben, I., and Rockmann, T.: Comparison of CH₄
1496 inversions based on 15 months of GOSAT and SCIAMACHY observations, *Journal
1497 of Geophysical Research-Atmospheres*, 118, 11807-11823, 2013.](#)

1498 [Nassar, R., Jones, D. B. A., Kulawik, S. S., Worden, J. R., Bowman, K. W., Andres, R.
1499 J., Suntharalingam, P., Chen, J. M., Brenninkmeijer, C. A. M., Schuck, T. J., Conway, T. J., and
1500 Worthy, D. E.: Inverse modeling of CO₂ sources and sinks using satellite observations of CO₂
1501 from TES and surface flask measurements, *Atmospheric Chemistry and Physics*, 11, 6029-6047,
1502 2011.](#)

1503 Parrish, D. F. and Derber, J. C.: [The National Meteorological Center's spectral statistical-
1504 interpolation analysis system](#)~~THE NATIONAL METEOROLOGICAL CENTERS SPECTRAL
1505 STATISTICAL INTERPOLATION ANALYSIS SYSTEM~~, *Monthly Weather Review*, 120,
1506 1747-1763, 10.1175/1520-0493(1992)120<1747:tnmcss>2.0.co;2, 1992.

1507 [Paulot, F., Jacob, D. J., Pinder, R. W., Bash, J. O., Travis, K., and Henze, D. K.: Ammonia emissions
1508 in the United States, European Union, and China derived by high-resolution inversion of
1509 ammonium wet deposition data: Interpretation with a new agricultural emissions
1510 inventory \(MASAGE NH₃\), *Journal of Geophysical Research-Atmospheres*, 119,
1511 4343-4364, 2014.](#)

1512 Peng, Z., Liu, Z., Chen, D., and Ban, J.: Improving PM_{2.5} forecast over
1513 China by the joint adjustment of initial conditions and source emissions with an ensemble Kalman
1514 filter, *Atmospheric Chemistry and Physics*, 17, 4837-4855, 10.5194/acp-17-4837-2017, 2017.

1515 Peng, Z., Lei, L., Liu, Z., Su, J., Ding, A., Ban, J., Chen, D., Kou, X., and Chu, K.: The impact of
1516 multi-species surface chemical observation assimilation on air quality forecasts in China,
1517 *Atmospheric Chemistry and Physics*, 18, 10.5194/acp-18-17387-2018, 2018.

1518 Peters, W., Jacobson, A. R., Sweeney, C., Andrews, A. E., Conway, T. J., Masarie, K., Miller, J. B.,
1519 Bruhwiler, L. M. P., Petron, G., Hirsch, A. I., Worthy, D. E. J., van der Werf, G. R., Randerson, J.
1520 T., Wennberg, P. O., Krol, M. C., and Tans, P. P.: An atmospheric perspective on North American
1521 carbon dioxide exchange: CarbonTracker, *Proceedings of the National Academy of Sciences of
1522 the United States of America*, 104, 18925-18930, 10.1073/pnas.0708986104, 2007.

1523 Peylin, P., Rayner, P. J., Bousquet, P., Carouge, C., Hourdin, F., Heinrich, P., Ciais, P., and
1524 contributors, A.: Daily CO₂ flux estimates over Europe from continuous atmospheric
1525 measurements: 1, inverse methodology, *Atmospheric Chemistry and Physics*, 5, 3173-3186,
1526 10.5194/acp-5-3173-2005, 2005.

1527 Purser, R. J., Wu, W. S., Parrish, D. F., and Roberts, N. M.: Numerical aspects of the application of
1528 recursive filters to variational statistical analysis. Part I: Spatially homogeneous and isotropic
1529 Gaussian covariances, *Monthly Weather Review*, 131, 1524-1535, 10.1175//1520-
1530 0493(2003)131<1524:naotao>2.0.co;2, 2003.

1531 [Quan, J., Liu, Q., Li, X., Gao, Y., Jia, X., Sheng, J., Liu, Y., 2015. Effect of heterogeneous aqueous](#)
1532 [reactions on the secondary formation of inorganic aerosols during haze events. *Atmospheric*](#)
1533 [*Environment* 122, 306-312.](#)

1534 Rabier, F., McNally, A., Andersson, E., Courtier, P., Uden, P., Eyre, J., Hollingsworth, A., and
1535 Bouttier, F.: The ECMWF implementation of three-dimensional variational assimilation (3D-Var).
1536 II: Structure functions, *Quarterly Journal Of the Royal Meteorological Society*, 124, 1809-1829,
1537 10.1256/smsqj.55002, 1998.

1538 [Reichle, R. H., McLaughlin, D. B., and Entekhabi, D.: Hydrologic data assimilation](#)
1539 [with the ensemble Kalman filter, *Monthly Weather Review*, 130, 103-114, 2002.](#)

1540 [Richardson, H., Basu, S., and Holtslag, A. A. M.: Improving Stable Boundary-Layer](#)
1541 [Height Estimation Using a Stability-Dependent Critical Bulk Richardson Number,](#)
1542 [*Boundary-Layer Meteorology*, 148, 93-109, 2013.](#)

1543 [Ruiz, J. and Pulido, M.: Parameter Estimation Using Ensemble-Based Data](#)
1544 [Assimilation in the Presence of Model Error, *Monthly Weather Review*, 143, 1568-](#)
1545 [*1582*, 2015.](#)

1546 Sarwar, G., Simon, H., Bhave, P., and Yarwood, G.: Examining the impact of heterogeneous nitril
1547 chloride production on air quality across the United States, *Atmospheric Chemistry and Physics*,
1548 12, 6455-6473, 10.5194/acp-12-6455-2012, 2012.

1549 [Sasaki, Y.: SOME BASIC FORMALISMS IN NUMERICAL VARIATIONAL ANALYSIS,](#)
1550 [*Monthly Weather Review*, 98, 875-&, 1970.](#)

1551 [Schneising, O., Buchwitz, M., Burrows, J. P., Bovensmann, H., Bergamaschi, P., and Peters, W.:](#)
1552 [Three years of greenhouse gas column-averaged dry air mole fractions retrieved from satellite -](#)
1553 [Part 2: Methane, *Atmospheric Chemistry and Physics*, 9, 443-465, 2009.](#)

1554 Schwartz, C. S., Liu, Z., Lin, H.-C., and Cetola, J. D.: Assimilating aerosol observations with a
1555 "hybrid" variational-ensemble data assimilation system, *Journal Of Geophysical Research-*
1556 *Atmospheres*, 119, 4043-4069, 10.1002/2013jd020937, 2014.

1557 Sekiyama, T. T., Tanaka, T. Y., Shimizu, A., and Miyoshi, T.: Data assimilation of CALIPSO aerosol
1558 observations, *Atmospheric Chemistry and Physics*, 10, 39-49, 10.5194/acp-10-39-2010, 2010.

1559 Shen, Y., Jiang, F., Feng, S., Zheng, Y., Cai, Z., and Lyu, X.: Impact of weather and emission changes
1560 on NO₂ concentrations in China during 2014–2019, *Environmental Pollution*, 269, 116163,
1561 10.1016/j.envpol.2020.116163, 2021.

1562 Shi, X. and Brasseur, G. P.: The Response in Air Quality to the Reduction of Chinese Economic
1563 Activities During the COVID-19 Outbreak, 47, e2020GL088070, 10.1029/2020gl088070, 2020.

1564 [Stanevich, I., Jones, D. B. A., Strong, K., Keller, M., Henze, D. K., Parker, R. J., Boesch, H., Wunch,](#)
1565 [D., Notholt, J., Petri, C., Warneke, T., Sussmann, R., Schneider, M., Hase, F., Kivi, R., Deutscher,](#)
1566 [N. M., Velazco, V. A., Walker, K. A., and Deng, F.: Characterizing model errors in chemical](#)
1567 [transport modeling of methane: using GOSAT XCH₄ data with weak-constraint four-dimensional](#)

1568 [variational data assimilation, Atmospheric Chemistry and Physics, 21, 9545-9572, 2021.](#)

1569 Stavrakou, T., Müller, J.-F., Boersma, K. F., De Smedt, I., and van der A, R. J.: Assessing the
1570 distribution and growth rates of NO_x emission sources by inverting a 10-year record of NO₂
1571 satellite columns, 35, 10.1029/2008gl033521, 2008.

1572 Sun, A. Y., Morris, A., and Mohanty, S.: Comparison of deterministic ensemble Kalman filters for
1573 assimilating hydrogeological data, *Advances in Water Resources*, 32, 280-292,
1574 10.1016/j.advwatres.2008.11.006, 2009.

1575 Takagi, H., Saeki, T., Oda, T., Saito, M., Valsala, V., Belikov, D., Saito, R., Yoshida, Y., Morino, I.,
1576 Uchino, O., Andres, R. J., Yokota, T., and Maksyutov, S.: On the Benefit of GOSAT Observations
1577 to the Estimation of Regional CO₂ Fluxes, *SOLA*, 7, 161-164, 10.2151/sola.2011-
1578 041, 2011.

1579 Tang, X., Zhu, J., Wang, Z. F., and Gbaguidi, A.: Improvement of ozone forecast over Beijing based
1580 on ensemble Kalman filter with simultaneous adjustment of initial conditions and emissions,
1581 *Atmospheric Chemistry And Physics*, 11, 12901-12916, 10.5194/acp-11-12901-2011, 2011.

1582 Tang, X., Zhu, J., Wang, Z. F., Wang, M., Gbaguidi, A., Li, J., Shao, M., Tang, G. Q., and Ji, D. S.:
1583 Inversion of CO emissions over Beijing and its surrounding areas with ensemble Kalman filter,
1584 *Atmospheric Environment*, 81, 676-686, 10.1016/j.atmosenv.2013.08.051, 2013.

1585 Wang, C., Lei, L., Tan, Z.-M., and Chu, K.: Adaptive Localization for Tropical Cyclones With
1586 Satellite Radiances in an Ensemble Kalman Filter, *Frontiers in Earth Science*, 8,
1587 10.3389/feart.2020.00039, 2020.

1588 [Wang, H., Jiang, F., Wang, J., Ju, W., and Chen, J. M.: Terrestrial ecosystem carbon flux estimated
1589 using GOSAT and OCO-2 XCO₂ retrievals, Atmospheric Chemistry and Physics, 19, 12067-
1590 12082, 2019a.](#)

1591 [Wang, N., Lyu, X., Deng, X., Huang, X., Jiang, F., and Ding, A.: Aggravating O₃ pollution due to
1592 NO_x emission control in eastern China, Science of The Total Environment, 677, 732-744, 2019b.](#)

1593 [Wang, Y. H., Hu, B., Ji, D. S., Liu, Z. R., Tang, G. Q., Xin, J. Y., Zhang, H. X., Song, T., Wang, L.
1594 L., Gao, W. K., Wang, X. K., and Wang, Y. S.: Ozone weekend effects in the Beijing-Tianjin-
1595 Hebei metropolitan area, China, Atmospheric Chemistry and Physics, 14, 2419-2429, 2014.](#)

1596 [Wang, Z., Li, Y., Dong, X., Sun, R., Sun, N., and Pan, L.: Analysis on weekend effect of air
1597 pollutants in urban atmosphere of Beijing, Journal of University of Chinese Academy of Sciences,
1598 32, 843-850, 2015.](#)

1599 [Wang, Z., Wang, W., Tham, Y.J., Li, Q., Wang, H., Wen, L., Wang, X., Wang, T., 2017. Fast
1600 heterogeneous N₂O₅ uptake and ClNO₂ production in power plant and industrial plumes
1601 observed in the nocturnal residual layer over the North China Plain. Atmospheric Chemistry and
1602 Physics 17, 12361-12378.](#)

1603 [Wecht, K. J., Jacob, D. J., Sulprizio, M. P., Santoni, G. W., Wofsy, S. C., Parker, R., Boesch, H., and
1604 Worden, J.: Spatially resolving methane emissions in California: constraints from the CalNex
1605 aircraft campaign and from present \(GOSAT, TES\) and future \(TROPOMI, geostationary\)
1606 satellite observations, Atmospheric Chemistry and Physics, 14, 8173-8184, 2014.](#)

1607 ~~Whitaker, J. S. and Hamill, T. M.: Ensemble data assimilation without perturbed observations,
1608 Monthly Weather Review, 130, 1913-1924, 10.1175/1520-
1609 0493(2002)130<1913:Edawpo>2.0.Co;2, 2002.~~

1610 Wu, H., Tang, X., Wang, Z., Wu, L., Li, J., Wang, W., Yang, W., and Zhu, J.: High-spatiotemporal-
1611 resolution inverse estimation of CO and NO_x emission reductions during emission control periods
1612 with a modified ensemble Kalman filter, *Atmospheric Environment*, 236,
1613 10.1016/j.atmosenv.2020.117631, 2020.

1614 Wu, W. S., Purser, R. J., and Parrish, D. F.: Three-dimensional variational analysis with spatially
1615 inhomogeneous covariances, *Monthly Weather Review*, 130, 2905-2916, 10.1175/1520-
1616 0493(2002)130<2905:tdvaws>2.0.co;2, 2002.

1617 [Yang, W., Li, J., Wang, W., Li, J., Ge, M., Sun, Y., Chen, X., Ge, B., Tong, S., Wang, Q., and Wang,
1618 Z.: Investigating secondary organic aerosol formation pathways in China during 2014,
1619 *Atmospheric Environment*, 213, 133-147, 2019.](#)

1620 Zhang, F., Weng, Y., Sippel, J. A., Meng, Z., and Bishop, C. H.: Cloud-Resolving Hurricane
1621 Initialization and Prediction through Assimilation of Doppler Radar Observations with an
1622 Ensemble Kalman Filter, *Monthly Weather Review*, 137, 2105-2125, 10.1175/2009mwr2645.1,
1623 2009a.

1624 [Zhang, L., Chen, Y., Zhao, Y., Henze, D. K., Zhu, L., Song, Y., Paulot, F., Liu, X., Pan, Y., Lin, Y.,
1625 and Huang, B.: Agricultural ammonia emissions in China: reconciling bottom-up and top-down
1626 estimates, *Atmospheric Chemistry and Physics*, 18, 339-355, 2018.](#)

1627 Zhang, Q., Streets, D. G., Carmichael, G. R., He, K. B., Huo, H., Kannari, A., Klimont, Z., Park, I.
1628 S., Reddy, S., Fu, J. S., Chen, D., Duan, L., Lei, Y., Wang, L. T., and Yao, Z. L.: Asian emissions
1629 in 2006 for the NASA INTEX-B mission, *Atmospheric Chemistry and Physics*, 9, 5131-5153,
1630 10.5194/acp-9-5131-2009, 2009b.

1631 Zhang, S., Zheng, X., Chen, J. M., Chen, Z., Dan, B., Yi, X., Wang, L., and Wu, G.: A global carbon
1632 assimilation system using a modified ensemble Kalman filter, *Geosci. Model Dev.*, 8, 805-816,
1633 10.5194/gmd-8-805-2015, 2015.

1634 Zhang, X., Liu, J., Han, H., Zhang, Y., Jiang, Z., Wang, H., Meng, L., Li, Y. C., and Liu, Y.: Satellite-
1635 Observed Variations and Trends in Carbon Monoxide over Asia and Their Sensitivities to Biomass
1636 Burning, *Remote Sensing*, 12, 10.3390/rs12050830, 2020.

1637 Zheng, B., Tong, D., Li, M., Liu, F., Hong, C., Geng, G., Li, H., Li, X., Peng, L., Qi, J., Yan, L.,
1638 Zhang, Y., Zhao, H., Zheng, Y., He, K., and Zhang, Q.: Trends in China's anthropogenic emissions
1639 since 2010 as the consequence of clean air actions, *Atmospheric Chemistry And Physics*, 18,
1640 14095-14111, 10.5194/acp-18-14095-2018, 2018.